

1 A stratigraphic approach to inferring depositional ages from
2 detrital geochronology data

3 Samuel A. Johnstone^{a*}, Theresa M. Schwartz^b, Christopher Holm-Denoma^c

4 ^aGeoscience and Environmental Change Science Center, U.S. Geological Survey, Denver, Colorado 80225,
5 USA

6 ^bDepartment of Geology and Geological Engineering, Colorado School of Mines, Golden, Colorado 80401,
7 USA

8 ^cGeology, Geophysics, and Geochemistry Science Center, U.S. Geological Survey, Denver, Colorado
9 80225, USA

10 * *corresponding author*: Samuel Johnstone, sjohnstone@usgs.gov

11 *This is a peer reviewed post print, please cite the published article as:* Johnstone, S., Schwartz, T. M., &
12 Holm-Denoma, C. S.. A Stratigraphic Approach to Inferring Depositional Ages From Detrital
13 Geochronology Data. <https://doi.org/10.3389/feart.2019.00057>

14 **Abstract**

15 With the increasing use of detrital geochronology data for provenance analyses, we have also
16 developed new constraints on the age of otherwise undateable sedimentary deposits. Because
17 a deposit can be no older than its youngest mineral constituent, the youngest defensible
18 detrital mineral age defines the maximum depositional age of the sampled bed. Defining the
19 youngest ‘defensible’ age in the face of uncertainty (e.g., analytical and geological uncertainty,
20 or sample contamination) is challenging. The current standard practice of finding multiple
21 detrital minerals with indistinguishable ages provides confidence that a given age is not an
22 artifact; however, we show how requiring this overlap reduces the probability of identifying the
23 true youngest component age. Barring unusual complications, the principle of superposition
24 dictates that sedimentary deposits must get younger upsection. This fundamental constraint
25 can be incorporated into the analysis of depositional ages in sedimentary sections through the
26 use of Bayesian statistics, allowing for the inference of bounded estimates of true depositional
27 ages and uncertainties from detrital geochronology so long as some minimum age constraints
28 are present. We present two approaches for constructing a Bayesian model of deposit ages,
29 first solving directly for the ages of deposits with the prior constraint that the ages of units
30 must obey stratigraphic ordering, and second describing the evolution of ages with a curve that
31 represents the sediment accumulation rate. Using synthetic examples we highlight how this
32 method preforms in less-than-ideal circumstances. In an example from the Magallanes Basin
33 of Patagonia, we demonstrate how introducing other age information from the stratigraphic
34 section (e.g., fossil assemblages or radiometric dates) and formalizing the stratigraphic context
35 of samples provides additional constraints on and information regarding depositional ages
36 or derived quantities (e.g., sediment accumulation rates) compared to isolated analysis of
37 individual samples.

1 Introduction

The age of a sedimentary deposit is no older than its youngest constituent. This fact, and the recent proliferation of detrital geochronology data to understand sedimentary provenance, have expanded the use of maximum depositional ages (MDAs) to constrain the ages of sedimentary deposits. With MDAs, researchers seek to limit the age of an otherwise undateable sedimentary deposit (e.g., a sandstone) using the ages of individual mineral grains, most commonly U-Pb ages of zircons determined by Laser Ablation-Inductively Coupled Plasma-Mass Spectrometry (LA-ICP-MS). The challenge to this approach is transforming the many individual dates of a detrital zircon study (tens to hundreds of grains are often dated per sample, see [Coutts et al., 2019](#); [Sharman et al., 2018](#)) to a single measure of the maximum age of the deposit. Analytical and geologic uncertainty in dating methods cause variability about the ‘true’ age of crystallization, such that any given measured age may be scattered about the true age of the rock. Repeated processing of samples in mineral separation facilities also introduces the possibility of potential contamination, as a single misplaced grain of sand could skew results. The imperfection of geologic chronometers means that in the case of radiometric dates, parent or daughter isotopes may be lost, resulting in an incorrect or inaccurate calculation of an age. In response to these challenges, a variety of methods have been developed to aggregate a suite of measured ages from a single detrital sample into a single estimate of the maximum age of the deposit ([Dickinson and Gehrels, 2009](#); [Coutts et al., 2019](#)).

In addition to being no older than its youngest constituent, the age of a sedimentary deposit is bracketed by the ages of deposits above and below it in a stratigraphic succession. A Geologist would refer to this as the principle of superposition. A Bayesian Statistician would call this valuable prior information. Superposition and Bayesian statistics have long been used to refine inferences about deposit ages that are based on geochronology ([Naylor and Smith, 1988](#); [Buck et al., 1992](#); [Christen et al., 1995](#)). The utility of these methods has resulted in the development of a number of computational tools to enable routine Bayesian analysis of suites of (primarily) radiocarbon ages ([Blaauw and Christen, 2005](#); [Parnell et al., 2008](#); [Haslett and Parnell, 2008](#); [Bronk Ramsey, 2009](#); [Blaauw, 2010](#); [Blaauw and Christeny, 2011](#), e.g.). Most commonly these tools are employed to make probabilistic assessments of the age of sedimentary intervals between dated horizons that record environmental changes of interest ([Parnell et al., 2011](#)). Radiocarbon calibration results in complicated probabilities of age, which is perhaps part of the reason for popularity of Bayesian methods ([Parnell et al., 2011](#)). Inferring depositional ages from detrital geochronology data provides a similar challenge. While some methods of calculating MDAs predict a gaussian uncertainty, that uncertainty is still only describing the limiting age and hence we cannot use observed detrital mineral ages alone to describe a normally-distributed probability of a true depositional age.

Here, we demonstrate the application of Bayesian statistics to the analysis of detrital geochronology data. Specifically, we attempt to formalize the existing, relative age constraints provided by superposition or cross-cutting relationships into the analysis of deposit ages in stratigraphic sections containing detrital geochronologic and other diverse age constraints. It is common practice to informally place the constraints provided by superposition into interpretations of deposit ages in order to bridge the divide between what we can infer from detrital geochronology samples (a maximum age) and the true age of deposition. However, formalizing this approach in a statistical model allows for the direct estimation of true depositional ages and their uncertainties from

82 collections of diverse geochronologic constraints.

83 We begin by summarizing our general approach and then with a discussion that follows from
84 Andersen (2005) on how likely it is to observe the youngest detrital mineral grains in a sample, and
85 thus the likelihood of calculating the best possible MDA constraint available from the analysis of a
86 single deposit. Then, we introduce a general model for the probability of a depositional age given
87 an observed suite of detrital geochronology ages within a deposit. We use synthetic examples to
88 demonstrate how Bayesian statistics allow for the incorporation of the principle of superposition
89 into the analysis of depositional ages, specifically allowing for the calculation of depositional ages
90 and uncertainty estimates from diverse geochronologic constraints (including limiting ages such as
91 those provided by detrital geochronology). We follow this with a real example from the Magallanes
92 basin of Patagonia (after Schwartz et al., 2017). In this example we demonstrate that the observed
93 chronology of stratigraphy in the Magallanes basin is consistent with the self-similar progradation
94 of a continental shelf-slope system with a topography that is consistent with observations from
95 analogous modern depositional systems. Thus, we show how added geologic context can refine our
96 interpretations of geochronology-based depositional ages.

97 2 Theory

98 2.1 Enforcing superposition in the inference of true depositional ages

99 Detrital geochronology samples are commonly collected alongside suites of other observations (e.g.,
100 Figure 1 A): information regarding stratigraphic position, notable fossil assemblages, and (often
101 sparse) age constraints from units that can be directly dated (e.g., ashes) within a sedimentary
102 succession. There are two strategies for incorporating the principle of superposition into age
103 determinations, directly modelling the ages of depositional events (e.g., Naylor and Smith, 1988;
104 Bronk Ramsey, 2009) and using observations that constrain the ages of units to model a curve
105 describing the stratigraphic accumulation through time (e.g., Blaauw and Christen, 2005; Parnell
106 et al., 2008; Haslett and Parnell, 2008; Bronk Ramsey, 2009; Blaauw, 2010; Blaauw and Christeny,
107 2011; Parnell et al., 2011).

108 Directly modelling the credible ages of units based on the geochronologic constraints available
109 and their stratigraphic relationship to one another is the simplest approach conceptually. The
110 premise of this approach (that the observed geology provides a strict relative ordering to deposits)
111 is easily transferable to other geologic scenarios where context provides constraints on the relative
112 age of samples (i.e., any cross-cutting relationship). Given n units in a sedimentary section that
113 contain age information, we seek to describe the probability of the age, t_i , of the geologic unit U_i ,
114 based on a series of observations, \mathbf{O} (Fig. 1 B). Here, our ‘observations’ are those data that we
115 collect that pertain to the age of a deposit. We refer to the probability of a set of ages for those
116 units, \mathbf{t} , given a set of j observations, as $p(\mathbf{t}|\mathbf{O})$, the *posterior* probability. Bayes rule gives:

$$p(\mathbf{t}|\mathbf{O}) \propto p(\mathbf{t})p(\mathbf{O}|\mathbf{t}) = p(\mathbf{t}) \prod_{i=0}^j p(O_i|t_i). \quad (1)$$

117 Here, $p(\mathbf{t})$ is our *prior* understanding of the probability of a set of n ages of stratigraphic units,
118 information we had before collecting our observations of unit ages. The *likelihood* of our observa-

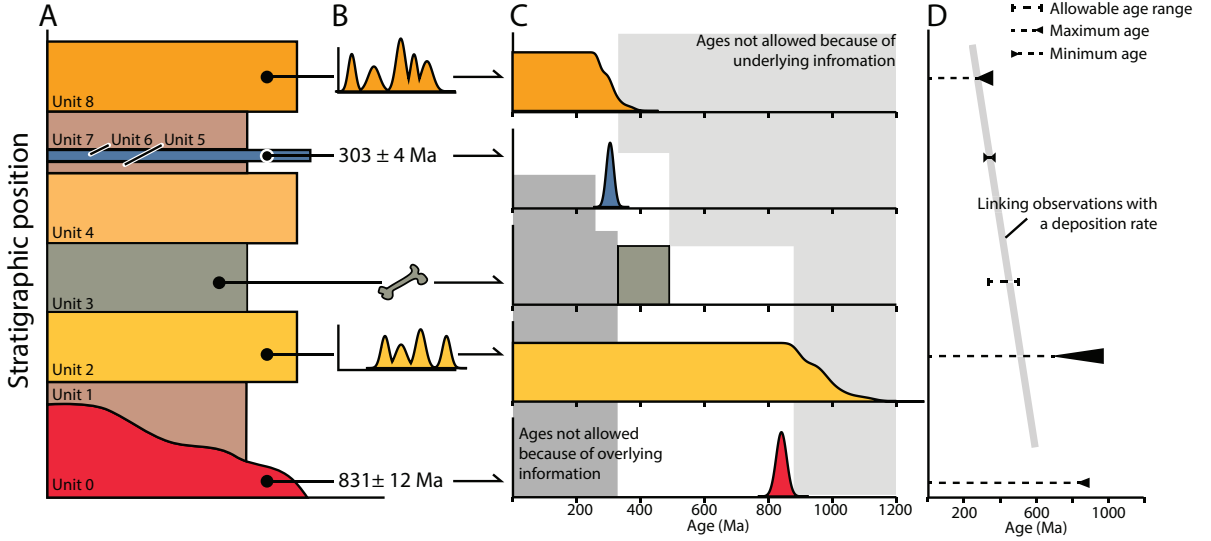


Figure 1: . Cartoon illustrating the use of sets of variable observations to constrain the timing of deposition. **A** shows a stratigraphic column where a series of observations, shown in **B**, were made that pertain to the ages of units within the section. **C** highlights the constraint on depositional age provided by each individual observation and the cumulative constraints provided by all observations in the section (shown in gray). In **D**, all of the individual observations are linked through a curve describing a constant-rate of uninterrupted sediment accumulation.

119 tions given a suite of modeled deposit ages is $p(\mathbf{O}|\mathbf{t})$, as shown in Figure 1 C. Conceptually, the
 120 *posterior* probability of \mathbf{t} reflects the probability of depositional ages *after* we have accounted for
 121 our observations. The *prior* probability is what we understood of the ages of units *before* analyzing
 122 our geochronologic data.

123 Some geologic units are directly dateable (e.g., ash deposits) and may result in normally dis-
 124 tributed *likelihoods* (e.g., Units 0 and 6, Fig. 1). Here, we consider fossil assemblages to limit the
 125 age of deposition to a range of ages (e.g., Unit 3, Fig. 1) with strict bounds based on the geologic
 126 timescale (Walker et al., 2018). While this provides a useful starting point, in reality the *likelihood*
 127 of observing a fossil at a particular time period is not a simple step function as depicted for Unit
 128 3 of Figure 1, as our knowledge of the timing of extinctions is not perfect and the preservation of
 129 fossils is not constant through time. We discuss the *likelihood* of a depositional age given a suite
 130 of detrital mineral ages more below, but the general form of the *likelihood* function is highlighted
 131 by Unit 2 and Unit 8 of Figure 1 C: probabilities are uniform for every age we are confident is
 132 younger than the youngest grain age, and then decline according to the mean ages, uncertainties,
 133 and overlap of young grains.

134 The simplest way to enforce the stratigraphic ordering of our samples is the statement that a
 135 sample cannot be older than the units below it (Fig. 1 C) (e.g., Naylor and Smith, 1988; Bronk
 136 Ramsey, 2009) ,

$$p(\mathbf{t}) = \begin{cases} 1, & \text{if } t_0 > t_1 > t_2 \dots t_{n-1} > t_n \\ 0, & \text{otherwise.} \end{cases} \quad (2)$$

137 When combined with age constraints from our observations, this stratigraphic, *prior* constraint
 138 on the ‘stacking’ of ages explicitly disallows those ages that would violate an age constraint from

139 under- or overlying material (Fig. 1 C). It is worth noting here that we are assuming that a single
 140 point in time, t_i , can characterize the age of a deposit from which a geochronologic constraint
 141 was established and that all the dated units represent distinct events; in other words deposition
 142 of the sampled unit was instantaneous. This is a reasonable assumption when the time it takes to
 143 form a deposit is much smaller than the precision of the chronometers used to date that deposit,
 144 but shorter timescales of deposition than the millions-of-year histories we consider here and more
 145 precise dating methods require more detailed consideration of events and the constraints within
 146 them (Bronk Ramsey, 2009).

147 Markov-chain Monte Carlo methods (MCMC) allow us to model depositional ages according
 148 to Eqn. 1 given a set of observations with differing descriptions of the probability of a given age
 149 (e.g., the different shapes to the curves in Fig. 1 C).

150 Alternatively, rather than model a suite of depositional ages directly, observations throughout
 151 the stratigraphic column can be linked through a sediment accumulation rate curve (Fig. 1 D).
 152 Here we use the phrase ‘stratigraphic accumulation rate’ rather than ‘deposition rate’ because we
 153 intend to characterize the time difference between measured intervals in a stratigraphic section,
 154 which may integrate variable deposition rates, small and unrecognized unconformities, and the
 155 effects of compaction. Modelling a stratigraphic accumulation rate curve has the distinct advantage
 156 of allowing for the assessment of ages and uncertainties of depths in the stratigraphic column that
 157 are undated, but may record important events (Parnell et al., 2011). As a result, tools such as
 158 such as BChron (Haslett and Parnell, 2008; Parnell et al., 2008), OxCal (Bronk Ramsey, 2009),
 159 and Bacon (Blaauw and Christeny, 2011) have been developed to enable routine incorporation of
 160 this analysis into investigations of sedimentary successions.

161 As an example, consider a constant sediment accumulation rate, $R [Lt^{-1}]$, that begins at the
 162 time of the lowest stratigraphic interval t_0 ; the age of unit i at the height $H_i [L]$ above the lowest
 163 stratigraphic unit is:

$$H_i = R(t_0 - t_i). \quad (3)$$

164 Because H_i can be measured from the stratigraphic section, this limits the model of depositional
 165 ages to two parameters, the sediment accumulation rate, R , and the timing of initial deposition,
 166 t_0 , such that $t_i = t_0 - \frac{H_i}{R}$. In this framework, we modify the parameters of interest in Eqn. 1,

$$p(t_0, R | \mathbf{O}) \propto p(t_0, R) p(\mathbf{O} | t_0, R). \quad (4)$$

167 In Equation 4, our *prior* probability, $p(t_0, R)$, would be assigned so that ages decrease upsection.

168 The choice of a linear sediment accumulation rate is arbitrary, and it is easy to see from Fig.
 169 1 how this can cause problems. For example, a period of non-deposition between Unit 1 and
 170 Unit 0 in Fig. 1 A seems to best describe the observed ages of these units. It is impossible to
 171 fit a linear sediment accumulation rate through all the constraints in the column with deposition
 172 beginning at 831 Ma, the measured age of Unit 0 (Fig. 1). Different forms to the sediment
 173 accumulation rate curve could be specified based on additional geologic context, and features such
 174 as unconformities could even be considered directly (e.g., Blaauw, 2010). Many existing age-
 175 depth models simulate stratigraphic accumulation rate curves in ways that allow a great deal of

176 flexibility in the determination of accumulation rates and how they fluctuate through time (see
177 Parnell et al., 2011, for a more detailed discussion of these approaches). For example, Bacon
178 (Blaauw and Christeny, 2011) allows for variations in deposition rates through time as dictated
179 by the observed age constraints (while enforcing monotonic accumulation of sediment) but can
180 introduce smoothness to stratigraphic accumulation rate curves by simulating and assigning a
181 *prior* probability to a term that governs a time period’s ‘memory’ of previous accumulation rates.

182 2.2 The search for the youngest grain

183 To incorporate detrital geochronology and the Bayesian approach in our characterization of depo-
184 sitional ages, we must characterize the *likelihood* of a true depositional age given a set of detrital
185 mineral ages (Eqn. 1). One of the most common methods for characterizing the formation age of
186 the youngest mineral grains is to compute the weighted mean (and its uncertainty) of the youngest
187 cluster of grains that overlaps within uncertainty (Coutts et al., 2019; Dickinson and Gehrels,
188 2009). Typically, the youngest cluster is only considered if it contains a minimum number of indi-
189 vidual dates, k_c , where k_c is commonly three or more (Coutts et al., 2019; Dickinson and Gehrels,
190 2009). The theory behind this approach is that a set of overlapping ages suggests that there is
191 a real age component present, rather than a single age being a fluke of the analysis or the result
192 of contamination. However, a concern with this approach is that requiring a certain number of
193 grains potentially ignores ages that are providing real depositional information, but may be fairly
194 uncommon and therefore rarely analyzed in a given sample. A question naturally follows from this:
195 how likely are we to actually observe k_c grains that came from the youngest unit when we date
196 n total grains? In other words, if we require k_c grains to calculate an MDA, how likely are we to
197 observe the true youngest age of a deposit’s detrital components?

198 To address this, we conceptualize each of our detrital geochronometer dates as representing a
199 lottery with one of two possible outcomes; a success or a failure. A success occurs when we date
200 a grain from that youngest unit, a failure occurs when we do not. As was previously recognized
201 by Andersen (2005), the question of how likely we are to identify a particular component age can
202 be characterized as a binomial experiment. Given that the youngest geologic unit contributed a
203 fraction of the total *dateable* grains deposited in a unit, f , the probability of any one date being a
204 ‘success’ is f and the probability of a ‘failure’ is $1 - f$. In most, if not all, ancient geologic settings,
205 it is impossible to know what f is before conducting a detrital geochronology study. The relative
206 contribution of detrital minerals from a young geologic source will depend on the average erosion
207 rate, concentration of minerals of interest in that unit (i.e., its ‘fertility’), the areal extent of the
208 youngest unit, and the mixing and transport of detrital sediments prior to deposition (Amidon
209 et al., 2005). Understanding any one of these important controls on f is difficult in an ancient
210 setting, let alone all of them. Nevertheless, we find it useful to define the quantity f as a means of
211 exploring MDAs. The probability of dating exactly k grains from the youngest unit out of a total
212 of n grains is given by the binomial distribution

$$p(k) = \binom{n}{k} f^k (1 - f)^{n-k}. \quad (5)$$

213 Here $\binom{n}{k}$ (read ‘ n choose k ’) is the binomial coefficient, which accounts for the number of ways

214 that k ‘successes’ and $n - k$ ‘failures’ could be organized in a series of n dates,

$$\binom{n}{k} = \frac{n!}{k!(n-k)!}. \quad (6)$$

215 A more appropriate question for the purpose of determining an MDA from a detrital sample is how
 216 likely are we to undersample the youngest age population, given that we set a criterion of dating
 217 k_c grains? We can consider the odds of sampling ‘enough’ young grains to calculate an MDA (e.g.,
 218 $p(k \geq k_c)$) by characterizing the sum of the odds of sampling too few grains. That is, if we
 219 decide we need three grains to calculate an MDA, the odds of not dating all three is the sum of the
 220 odds of dating only two grains from the youngest unit, dating one grain from the youngest unit,
 221 and dating no grains from the youngest unit. Specifically, the odds of dating enough grains for an
 222 MDA is given as one less the probability of *not* dating enough,

$$p(k \geq k_c) = 1 - \sum_{i=0}^{k_c-1} \binom{n}{i} f^i (1-f)^{n-i}. \quad (7)$$

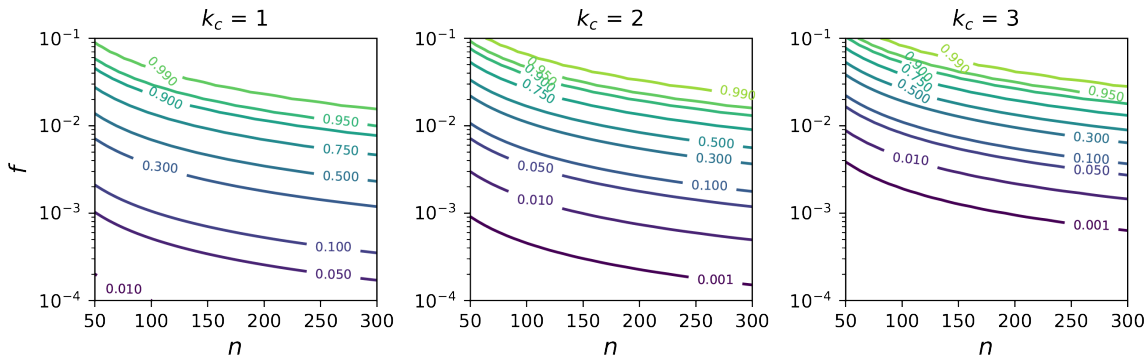


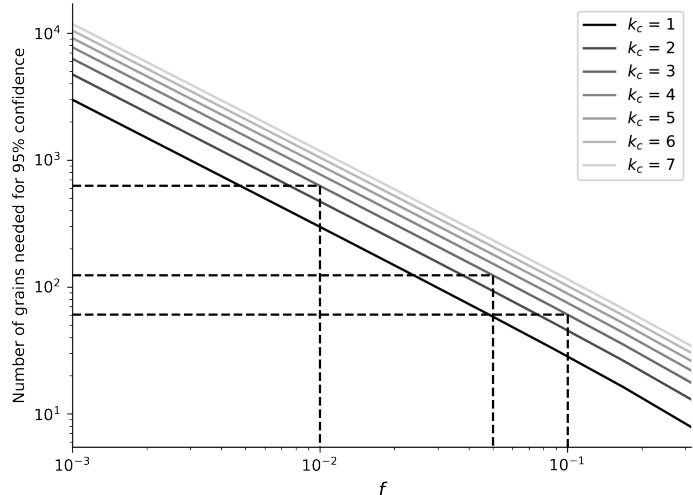
Figure 2: Probabilities of dating enough grains from the youngest constituent to compute an MDA, given that k_c grains are required to compute an MDA and that the grains belonging to the youngest age component constitutes a fraction f of all dateable grains (Eqn. 7). The three panels show probability contours for $k_c = 1, 2, \& 3$.

223 If we require using at least three grains to determine an MDA, then we lower the probability
 224 that we will actually resolve the youngest MDA (e.g., Fig. 2, Dickinson and Gehrels, 2009). Rather
 225 than viewing the probability field of Fig. 2, we can directly ask how many grains are needed such
 226 that in 95% of cases we would date at least k_c grains from the youngest age component (Fig. 3).
 227 In cases where these youngest grains make up 1% or less of all dateable minerals, we would only
 228 expect to date three of the same grains 95% of the time if we were to date around 630 grains (Fig.
 229 2 & 3). If the youngest detrital minerals only make up 1% of all dateable minerals, analyses of
 230 ~ 100 grains would only resolve the youngest MDA $\sim 10\%$ of the time. Even if we only require two
 231 dates from the same youngest unit (Fig. 2, $k_c = 2$), it is only in cases where those youngest grains
 232 represent $\sim 5\%$ of all grains that we would expect to observe two of them in 95% of experiments
 233 where we dated 100 grains. While a simplification, Eqn. 5 reflects results from previous work that
 234 large numbers of analyses are essential for confidently resolving the youngest population of grains
 235 through repeated analyses (e.g., Coutts et al., 2019).

236 Equation 5 and Fig. 2 highlight another concern with methods that seek to quantify an MDA
 237 through averaging replicate measurements and assigning an uncertainty to the resulting MDA:
 238 that the resulting uncertainty is not a actually a measure of confidence in the MDA, but rather a

239 measure of the similarity and precision of those ages that were selected as representative. In other
 240 words, the 2σ bound on pooled MDA methods does not reflect 95% confidence in the youngest
 241 grains in a population being drawn from that interval, because we may have had a very small
 242 chance of observing the youngest grains to begin with (Fig. 2).

Figure 3: How many grains should be dated to be 95% confident that we would date at least k_c grains from the youngest source of grains? The solid lines provide this recommendation as a function of f , the fraction of dateable mineral grains from the youngest source. In practice, it is unlikely that this quantity can be known. The dashed lines represent specific recommendations for if $f = 10, 5, \& 1\%$. In 95% of cases where you date $\sim 60, \sim 120$, and ~ 630 grains, at least 3 grains will be dated from sources that contributed 10, 5, & 1% of all the dateable minerals.



243 2.3 Transforming maximum depositional ages into predictions of true 244 depositional age

245 It is challenging, if not impossible, to identify an infallible method to compute a single MDA from
 246 a series of ages; how can you appropriately characterize confidence in establishing the age of the
 247 youngest material when it is impossible to know how common that material should be (e.g. f of
 248 Fig. 2)? How likely is it that your sample was contaminated or that a mineral grain retained, and
 249 you measured, all of its parent and daughter isotopes?

250 To compute MDAs we rely on an approach presented by Keller et al. (2018). We model the
 251 timing of last crystallization as the truncation of a prior expectation of the probability of zircon
 252 ages. Given a prior understanding of the relative proportions of dateable grains formed throughout
 253 mineral growth, f_{xtal} , we can modify that distribution by truncating the probability of observing
 254 an age, t_{obs} , greater than the time at which the first mineral crystallized, t_{sat} , and less than the
 255 time at which the youngest crystal could have formed, t_e ,

$$p(t_{obs}|t_e, t_{sat}) = \begin{cases} 0, & \text{if } t_{obs} < t_e \\ 0, & \text{if } t_{obs} > t_{sat} \\ f_{xtal}/(t_{sat} - t_e), & \text{otherwise.} \end{cases} \quad (8)$$

256 Keller et al. (2018) present results constructing f_{xtal} from expectations derived from a ther-
 257 modynamic model of a steadily cooling magma body, from kernel density estimates derived from
 258 observed ages within the dated unit, and with a uniform prior that makes no assumptions about
 259 the relative timing of crystallization (e.g., $f_{xtal} = 1$ in Eqn. 8). Here, we utilize the uniform prior
 260 approach, as detrital distributions likely integrate complex histories of crystal growth and recycling
 261 which we don't presume to be able to fully characterize. We utilize a Markov-Chain Monte Carlo

262 Model (Foreman-Mackey et al., 2013) to infer the *posterior* distributions of t_e and t_{sat} , although
 263 for MDA analysis we are only interested in the former. In this approach, a series of ‘walkers’ take
 264 random steps about an initial guess of parameters such that they first explore the parameter space
 265 (a ‘burn-in’ phase) and then take steps such that the frequency of parameters sampled at each step
 266 mirrors the *posterior* probability of those parameters. From initial guesses of t_e and t_{sat} that vary
 267 randomly about the youngest and oldest ages in a sample, respectively, we update these estimates
 268 over 700 steps taken by an ensemble sampler with 100 walkers and trim a burn-in period of 200
 269 steps from the sample-chain constructed by each walker, resulting in 50,000 samples characterizing
 270 the *posterior* of t_e and t_{sat} .

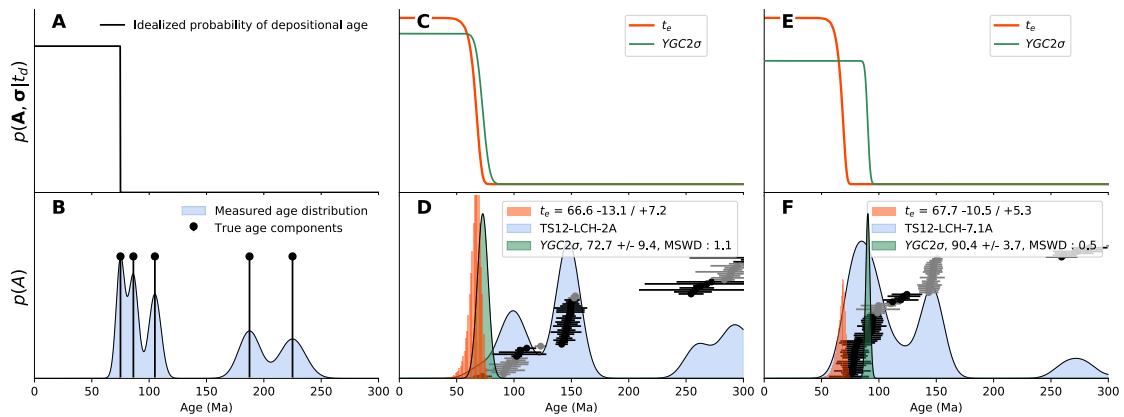


Figure 4: . The top row highlights probabilities of observing a set of detrital ages \mathbf{A}, σ , given an age of the deposit t_d , whereas the bottom row shows our observations. Panels **A** & **B** show an idealized example, where we have absolute confidence that we have characterized the true formation age of constituent minerals, shown in **B**, so that the deposit is equally likely to be any age younger than the youngest age component. **B** also highlights an example of how we might have characterized the distribution of ages of this example based on measurements. **D** & **F** highlight real detrital zircon geochronology data, whereas **C** & **E** show example likelihood functions for the depositional age of these samples based on two methods for determining MDAs from observed data. In **D** & **F**, a Gaussian kernel density estimate with a 10 Ma bandwidth (Vermeesch, 2012) is shown alongside the observed ages and their uncertainties (shown as circles with lines showing the 95% confidence intervals). Individual ages are shown in alternating colors to indicate different groups. Groups are defined based on overlap of the 2σ confidence interval of the youngest grain in that group.

271 Examples of MDAs calculated with the weighted mean of the youngest grain cluster overlapping
 272 at 2 sigma (YGC2 σ , Dickinson and Gehrels, 2009) and t_e estimates are shown in Figure 4 D & F.
 273 In the example shown in Figure 4 D, there is relatively good agreement between the two samples,
 274 as an isolated cluster of three young grains defines the MDA calculated with the YGC2 σ method.
 275 However, the example shown in Figure 4 F shows how the two methods can deviate; an over-
 276 dispersed but overlapping cluster of grains pulls the YGC2 σ MDA toward older values, while t_e
 277 is limited by the youngest observed grains. Unlike the weighted mean approach, characterizing t_e
 278 does not require the selection of a sub-population of observed ages and is therefore able to produce
 279 reliable estimates without interpretations of groupings. For these reasons, in addition to those
 280 discussed in Keller et al. (2018), we use t_e to characterize MDAs from here out in the text.

281 More important than the MDA method used is the recognition that when using detrital
 282 geochronology data to understand geologic histories, it is the true depositional age that we are
 283 typically interested in. The bottom row of Figure 4 highlights the probabilities of crystallization
 284 ages. The top row of Figure 4 highlights our focus in the manuscript, how likely is it that we

285 would have observed a suite of detrital mineral ages if the deposit were of a certain age? We refer
 286 to this as $p(\mathbf{A}, \boldsymbol{\sigma}|t_d)$, the *likelihood* of a series of ages, \mathbf{A} , and their associated uncertainties, $\boldsymbol{\sigma}$,
 287 given a depositional age t_d . If we knew the true age components of our sample (Fig. 4 B), then
 288 $p(\mathbf{A}, \boldsymbol{\sigma}|t_d)$ would be equal for all ages younger than the youngest true component age (Fig. 4 A),
 289 but there is no chance (e.g. $p = 0$) that one of these true component ages could be less than
 290 t_d . In some situations, for example known proximity to an active arc, future work may wish to
 291 consider the situation where true depositional ages close to those of the youngest zircons are more
 292 likely than those associated with large lags between crystallization and deposition. We ignore this
 293 special case and just consider detrital ages to define upper bounding ages. Our characterization of
 294 the youngest mineral ages is subject to uncertainties associated with our measurements and our
 295 ability to identify the youngest mineral ages from within a complex population (Fig. 4 C-F). Here
 296 we assume that we can characterize the *likelihood* of observing a set of detrital mineral ages given
 297 a true depositional age, $p(\mathbf{A}, \boldsymbol{\sigma}|t_d)$, based entirely on the probability that the depositional age is
 298 less than the MDA,

$$p(\mathbf{A}, \boldsymbol{\sigma}|t_d) = \frac{1 - \int_0^{t_d} p(t|MDA)dt}{\int_0^{4.5Ga} 1 - p(t|MDA)dt}. \quad (9)$$

299 Here, $p(t|MDA)$ refers to the probability of a particular age, t , characterizing an MDA. In
 300 the case of YGC2 σ this would be governed by a normal distribution, but the probabilities of t_e
 301 are not necessarily normally distributed. The numerator in Equation 9 is just a mirror image of
 302 the cumulative density function of the MDA (Fig. 4 A,C, & E). The denominator in Equation 9
 303 integrates over the age of the earth to ensure that the probabilities of all possible ages integrate
 304 to one. Plotting Equation 9 emphasizes that these are indeed only *maximum* depositional ages;
 305 providing no information about the lower bound on possible depositional ages (Fig. 4 C & E). It
 306 is only through context with other neighboring samples that we can determine bound estimates of
 307 true depositional ages.

308 2.4 Examples of depositional age and uncertainty inference

309 We use synthetic examples to demonstrate how the depositional ages inferred using Eqn. 1 respond
 310 given ideal and, perhaps, more common scenarios with detrital geochronology. Figure 5 highlights
 311 a stratigraphic section from which five geochronology samples were collected. The lower four are all
 312 detrital geochronology samples, while the upper sample is a direct date of an ash bed (this sample
 313 provides a lower-limit to the underlying ages). Figure 5 B highlights a well-behaved example; the
 314 best-case scenario where the youngest grains from a suite of detrital geochronology samples nearly
 315 overlap or young upsection and are close to overlapping with the absolute age constraint at the
 316 top of the section (Fig. 5 B). Figures 5 C & D provide increasingly complicated scenarios: in C
 317 not all youngest grain ages decrease upsection, and in D there is a large time gap between the
 318 youngest grains of the basal sample and the second sample up from the bottom of the section. The
 319 examples shown in Figures 5 C & D are derived by incrementing all the observed ages in a subset
 320 of samples shown in Figure 5 B.

321 To integrate the individual age constraints informed by observations within individual deposits
 322 (e.g., the detrital geochronology data and age of the upper ash that inform the likelihood of a
 323 unit's age, $p(O|t)$ of Eqn. 1) with the constraints dictated by stratigraphic ordering (Eqn. 2), we

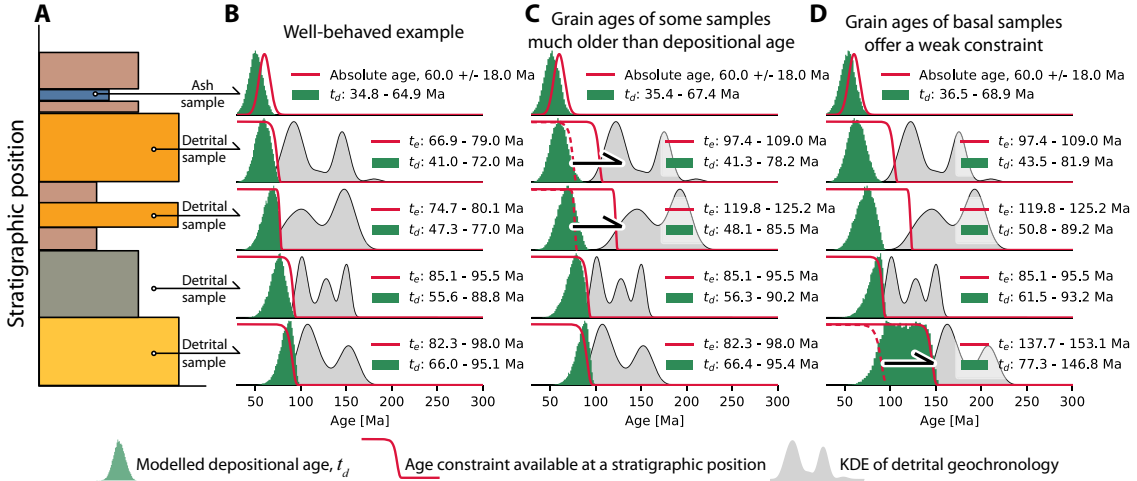


Figure 5: A synthetic example of a stratigraphic section (A) with five geochronologic constraints. The bottom four age constraints are from detrital geochronology samples, the top sample represents a dated ash bed (or any other deposit that can be directly dated). The plot in column B is an idealized example; plots in columns C and D are results given modifications to B. In B-D each row shows the *posterior* probability of the depositional age of that unit as a green histogram of MCMC samples with 50 evenly spaced bins, the *likelihood* of a depositional age given the data available for that deposit, and for detrital geochronology sample a KDE constructed with a gaussian kernel with a bandwidth equal to the mean 2σ uncertainty of samples. The black arrows in C & D show the datasets that were perturbed from the case shown in B. In each plot of model results, the legend indicates the 95% credible interval for the modelled true depositional age t_d and, for detrital geochronology samples, the MDA, t_e , determined with the approach of Keller et al. (2018).

324 utilize a Monte Carlo sampling approach. We make a guess of the age for each sample and then
 325 evaluate both its *prior* (Eqn. 2) and *likelihood* (e.g., Eqn. 1, Fig. 7). Specifically, we employ
 326 a Bayesian, MCMC approach with an affine-invariant ensemble sampler (Foreman-Mackey et al.,
 327 2013). In each iteration, a series of ‘walkers’ (each walker makes parameter guesses and evaluates
 328 them) takes a ‘step’ by evaluating a suite of parameters (e.g., the vector of true depositional
 329 ages \mathbf{t}). In the MCMC approach, the suite of guessed ages is chosen such that over time, the
 330 frequency with which ages are sampled mirrors the *posterior* probability (Foreman-Mackey et al.,
 331 2013; VanderPlas, 2014). For detrital samples, we first model the posterior of t_e and use this
 332 to numerically evaluate Eqn. 9. For this work, we ignore all grain ages older than 200 Ma in
 333 MCMC models of t_e . We run the MCMC models of t_d with 200 walkers that each take a total
 334 of 1,200 steps, and we trim the first 400 steps from each walker to allow for a ‘burn-in’ phase of
 335 the model where the sampler explores the parameter space around the initial guesses. Because
 336 of the stiff constraints imposed by stratigraphic ordering, we find that having a large number of
 337 samples characterizing the burn-in phase can be necessary to allow the model to fully explore the
 338 parameter space. Although we do not explore this concept here to maintain simplicity, the true
 339 depositional age also limits t_e , providing additional prior information that could be exploited if
 340 one simultaneously modelled values of t_e and t_d in a stratigraphic succession.

341 In the well-behaved example of Figure 5 B, we are able to predict comparable uncertainties (a
 342 95% credible interval of 30 Ma) for all samples despite only having a single absolute age constraint.
 343 The other way of viewing this, is that we are able to propagate the confidence we have from the
 344 directly dated sample into predictions of true depositional ages lower in the section.

345 Having some samples that do not contain MDAs close to the true depositional age does not

346 necessarily substantively impact our predicted depositional ages (Fig. 5 C). While the top two
347 detrital samples in Figure 5 C have much older youngest grains than those in Figure 5 B, the
348 predicted true depositional ages for these samples are only marginally older in example C. This is
349 because the upper samples did not provide much information that was not already available from
350 one of the lowermost two samples due to the overlap in t_e within these deposits (Fig. 5).

351 In Figure 5 D, the ages of the youngest grains in the basal sample are much older than the
352 youngest grains in the next sample upsection. This results in a broad, flat-topped posterior proba-
353 bility of true depositional ages because there is an extensive region between where overlying samples
354 provide information limiting the youngest ages and the grains provided in this sample limit the
355 oldest allowable age. The change in ages of the basal sample also impacts the credible intervals
356 of ages in all the overlying samples (allowing the upper bounds of most samples to increase by 4
357 Ma). This is reflecting the complex covariances that exist between the modelled true depositional
358 ages of samples, and the cascade of information that propagates through the prior constraint of
359 superposition. If the upper bounding absolute constraint was not present (and there were no other
360 constraints available to provide minimum bounds on ages), then all the modelled *posterior* proba-
361 bilities of true depositional ages would be broad plateaus, similar to that in the bottom sample of
362 Figure 5 D, but extending all the way to the present

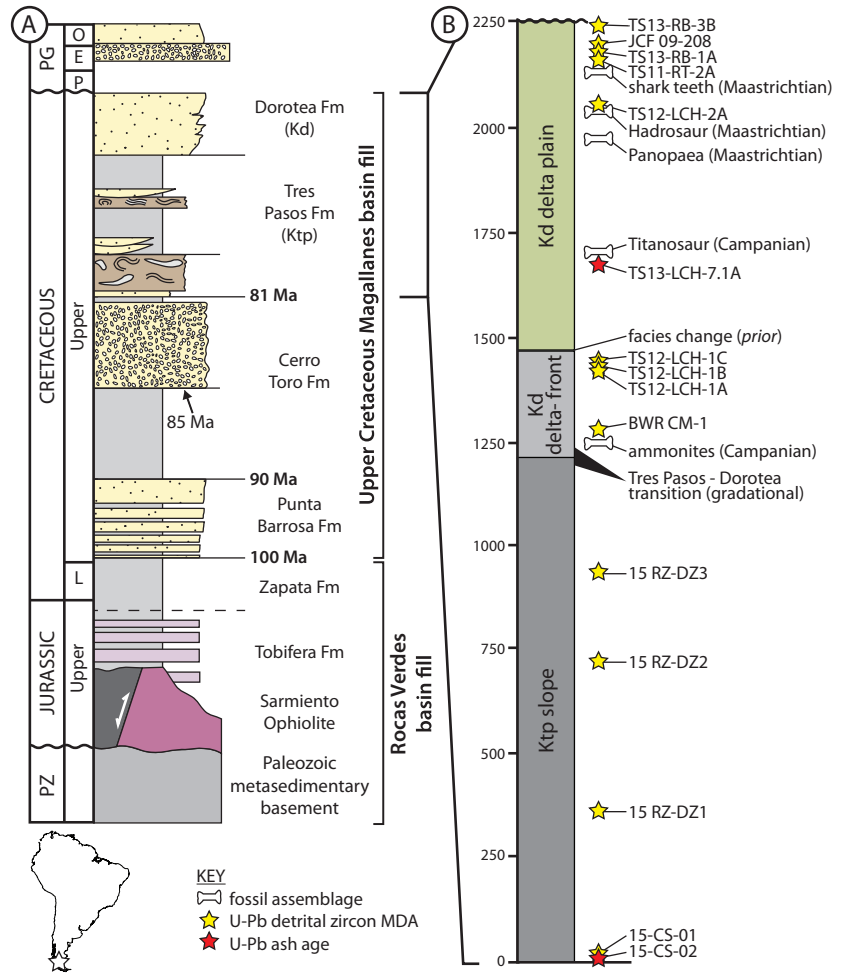
363 The other phenomenon highlighted by the examples in Figure 5 is how detrital geochronology
364 can refine the age estimates provided by direct dating. The uppermost age in these examples has
365 a broad uncertainty, but in Figure 5 B, the median value inferred from the depositional age model
366 (t_d) is shifted to be younger than the mean age of the absolute date. In Figure 5 B, the underlying
367 detrital geochronology samples provide information that shifts this sample to younger values, but
368 as the constraints provided by detrital geochronology are relaxed (in Figure 5 C & D), the *posterior*
369 estimate of t_d from the depositional age model becomes closer to the assigned absolute age.

370 3 Application to the Magallanes basin, Patagonia

371 3.1 Geologic setting and data exposition

372 The Magallanes basin is a retroarc foreland basin that formed during Late Cretaceous to Neo-
373 gene uplift of the southern Andes (Wilson, 1991). The foreland basin is floored by attenuated,
374 transitional-oceanic crust associated with the Jurassic-Early Cretaceous Rocas Verdes extensional
375 basin (Dalziel et al., 1974; Dalziel, 1981; Biddle et al., 1986; Wilson, 1991). Loading and flexure
376 of the dense, attenuated crust facilitated the formation of a deep-marine foredeep (Natland, 1974;
377 Fosdick et al., 2014), which accumulated more than 4 km of deep-marine basin floor to slope de-
378 posits (Punta Barrosa, Cerro Toro, and Tres Pasos Formations; Biddle et al., 1986; Romans et al.,
379 2010; Fosdick et al., 2011) that are overlain by up to 1 km of shelfal deposits (Dorotea Formation;
380 Schwartz and Graham, 2015) during Late Cretaceous time (Fig. 6). The uppermost deep-marine
381 deposits (Tres Pasos Formation; Fig. 6) and overlying shelfal deposits (Dorotea Formation; Fig. 6)
382 record shoaling in the foredeep between ca. 80-65 Ma, and together represent a genetically linked
383 shelf and slope that prograded southward along the axis of the Magallanes foredeep (Macellari
384 et al., 1989; Covault et al., 2009; Hubbard et al., 2010; Schwartz and Graham, 2015; Daniels et al.,
385 2018a; Schwartz et al., 2017).

Figure 6: Stratigraphic context for the zircon data modeled in this paper. (A) Simplified stratigraphic column for the Rocas Verdes and Magallanes basin fill in southern Chile, between approximately 51° 30' S and 50° 30' S (modified from Fosdick et al., 2011; Schwartz et al., 2017; Daniels et al., 2018a,b). Numeric ages in bold indicate well-established radiometric ages for major lithostratigraphic boundaries in the basin fill (after Daniels et al., 2018a,b). (B) Highly simplified, composite stratigraphic column for the Tres Pasos and Dorotea Formations at approximately 50° 45' S, which record shoaling in the Magallanes foredeep from bathyal to nonmarine environments through the successive deposition of progradational slope, delta-front and delta-plain deposits (after Schwartz et al., 2017; Daniels et al., 2018a). The stratigraphic positions of all available ash, detrital zircon, and fossil age constraints are indicated to the right of the column.



386 As a whole, the Magallanes foreland basin fill is well-constrained based on lithostratigraphic
 387 correlations, radiometric dates from ashes, and MDAs from detrital zircon samples (Fildani and
 388 Hessler, 2005; Romans et al., 2010; Bernhardt et al., 2011; Fosdick et al., 2011; Malkowski et al.,
 389 2017; Schwartz et al., 2017; Daniels et al., 2018a). Ashes are relatively abundant in the deep-marine
 390 phase of the basin fill (e.g., Fildani and Hessler, 2005; Bernhardt et al., 2011; Fosdick et al., 2011;
 391 Malkowski et al., 2017), but have not been observed above the base of the Tres Pasos Formation
 392 (Daniels et al., 2018a; Schwartz et al., 2017). Detrital zircon MDAs in the deep-marine section
 393 have been shown to closely overlap with stratigraphically adjacent ash ages (Bernhardt et al., 2011;
 394 Malkowski et al., 2017), supporting connectivity between the active Patagonian arc and foredeep as
 395 well as rapid transfer of volcanogenic sediment from the arc to the retroarc foreland basin (Schwartz
 396 et al., 2017). In addition, most detrital zircon MDAs from the shallow-marine section exhibit
 397 apparent younging up-section, supporting continued connectivity between the arc and foredeep
 398 through time and suggesting that MDAs may closely track true depositional ages of the deposits
 399 (Daniels et al., 2018a; Schwartz et al., 2017). In addition to radiometric age constraints, the
 400 Dorotea Formation contains relatively abundant fossil assemblages including ammonites, bivalves,
 401 shark teeth, and dinosaurs (Schwartz et al., 2017).

402 Lithostratigraphically, we simplify the 2.25 km-thick Tres Pasos-Dorotea depositional system
 403 into three conformable lithofacies assemblages: 1) mudstone-dominated slope clinoforms of the
 404 Tres Pasos Formation (1,200 m thick) that downlap onto basin-floor deposits of the Cerro Toro

405 Formation; 2) sandstone-dominated delta-front clinoforms of the Dorotea Formation (300 m thick)
406 that interfinger with topsets of the Tres Pasos Formation; and 3) heterolithic delta-plain deposits
407 of the Dorotea Formation(750 m thick, Fig. 6, Schwartz et al., 2017). Figure 6 shows the vertical
408 distribution of twenty existing age constraints for the Tres Pasos-Dorotea succession (compiled from
409 Daniels et al., 2018a; Schwartz et al., 2017): 1) one ash at the base of the Tres Pasos Formation;
410 2) fourteen detrital zircon samples that are distributed throughout the Tres Pasos and Dorotea
411 formations, one of which (TS12-LCH-7.1A) is interpreted as a fluviially reworked ash; and 3) five
412 fossil assemblages from the Dorotea Formation (Fig. 6, Table 1).

413 The Tres Pasos-Dorotea succession provides a unique opportunity to test our proposed modeling
414 framework for depositional ages for two reasons. First, this example includes abundant and varied
415 age constraints that are relatively evenly distributed throughout the > 2 km succession of strata,
416 but a relatively limited number of them (2 of 20) are expected to directly record the timing of
417 deposition. As a result, we can explore how well the modeling framework can refine estimates of the
418 timing of deposition provided by different sets of observations. Second, detailed sedimentological
419 comprehension of the Tres Pasos-Dorotea depositional system provides confidence in the relative
420 stratigraphic position of various age constraints and in the depositional environment, from which
421 we can construct an informed expectation for the form of a sedimentation rate curve. In the two
422 sections that follow, we explore how both the constraints of stratigraphic ordering (Eqn. 2, Fig.
423 1 C) and a sediment accumulation rate curve (Fig. 1 D) refine our models of depositional ages
424 based on geochronology data. For all detrital zircon geochronology samples we recompute an MDA
425 (following Keller et al., 2018, , see above) independent of modelling t_d , but for samples where direct
426 age constraints are available we describe the *likelihood* of depositional ages using the reported ages
427 and uncertainties of the presenting studies rather than reanalyzing the data ourselves (Table 1).

Sample	Original Source	Constraint type	Age constraint (Ma)	Stratigraphic Height (m)
TS13-RB-3B	Schwartz et al., 2017	DZ, 28 grains <200 Ma	<92 (+ 6 / - 10)	2245
JCF 09-208	Fosdick et al., 2015	DZ, 83 grains <200 Ma	<69 (+ 2 / - 4)	2225
TS13-RB-1A	Schwartz et al., 2017	DZ, 53 grains <200 Ma	<69 (+ 2 / - 4)	2200
TS11-RT-2A	Schwartz et al., 2017	DZ, 55 grains <200 Ma	<68 (+ 3 / - 7)	2180
Shark teeth	Schwartz et al., 2017	Fossil, Maastrichtian	66.0 - 72.1	2175
TS12-LCH-2A	Schwartz et al., 2017	DZ, 42 grains <200 Ma	<70 (+ 6 / - 8)	2075
Hadrosaur	Schwartz et al., 2017	Fossil, Maastrichtian	66.0 - 72.1	2060
Panopaea	Schwartz et al., 2017	Fossil, Maastrichtian	66.0 - 72.1	1950
Titanosaur	Schwartz et al., 2017	Fossil, Campanian	72.1 - 83.6	1670
TS13-LCH-7.1A	Schwartz et al., 2017	Reworked ash	78.0±3.6	1650
TS12-LCH-1C	Schwartz et al., 2017	DZ, 44 grains <200 Ma	<75 (+ 4 / - 8)	1420
TS12-LCH-1B	Schwartz et al., 2017	DZ, 52 grains <200 Ma	<81 (+ 2 / - 5)	1410
TS12-LCH-1A	Schwartz et al., 2017	DZ, 68 grains <200 Ma	<86 (+ 4 / - 5)	1400
BWR CM-1	Romans et al., 2010	DZ, 30 grains <200 Ma	<93 (+ 3 / - 7)	1300
ammonites	Schwartz et al., 2017	Fossil, Campanian	72.1 - 83.6	1250
15-RZ-DZ3	Daniels et al., 2018	DZ, 118 grains <200 Ma	<86 (+ 3 / - 4)	900
15-RZ-DZ2	Daniels et al., 2018	DZ, 150 grains <200 Ma	<78 (+ 2 / - 3)	725
15-RZ-DZ1	Daniels et al., 2018	DZ, 190 grains <200 Ma	<82 (+ 3 / - 3)	350
15-CS-01	Daniels et al., 2018	DZ, 158 grains <200 Ma	<83 (+ 3 / - 3)	10
15-CS-02	Daniels et al., 2018	Ash	80.5±0.6	0

Table 1: Summary of data sources and ages constraints used in modelling depositional ages of the Magallanes-Austral Basin. Detrital zircon (DZ in table) age constraints are reported as the median, and deviation to the lower 2.5th and upper 97.5th percentiles of MCMC samples of t_e (i.e., the 95% credible interval). Direct dates are reported as means and 2σ uncertainties. We follow the interpretation of Schwartz et al. (2017) that TS13-LCH-7.1A, collected from a reworked ash, can be interpreted as syndepositional. The number of grains reported in the ‘constraint type’ field references those grains less than 200 Ma old that we consider when modelling t_e , kernel density estimates for detrital geochronology data are shown in Fig. 7 & 10. Age ranges for fossil assemblages are use the timescale of Walker et al. (2018).

428 **3.2 Modeling the ages of stratigraphy with stratigraphic ordering**

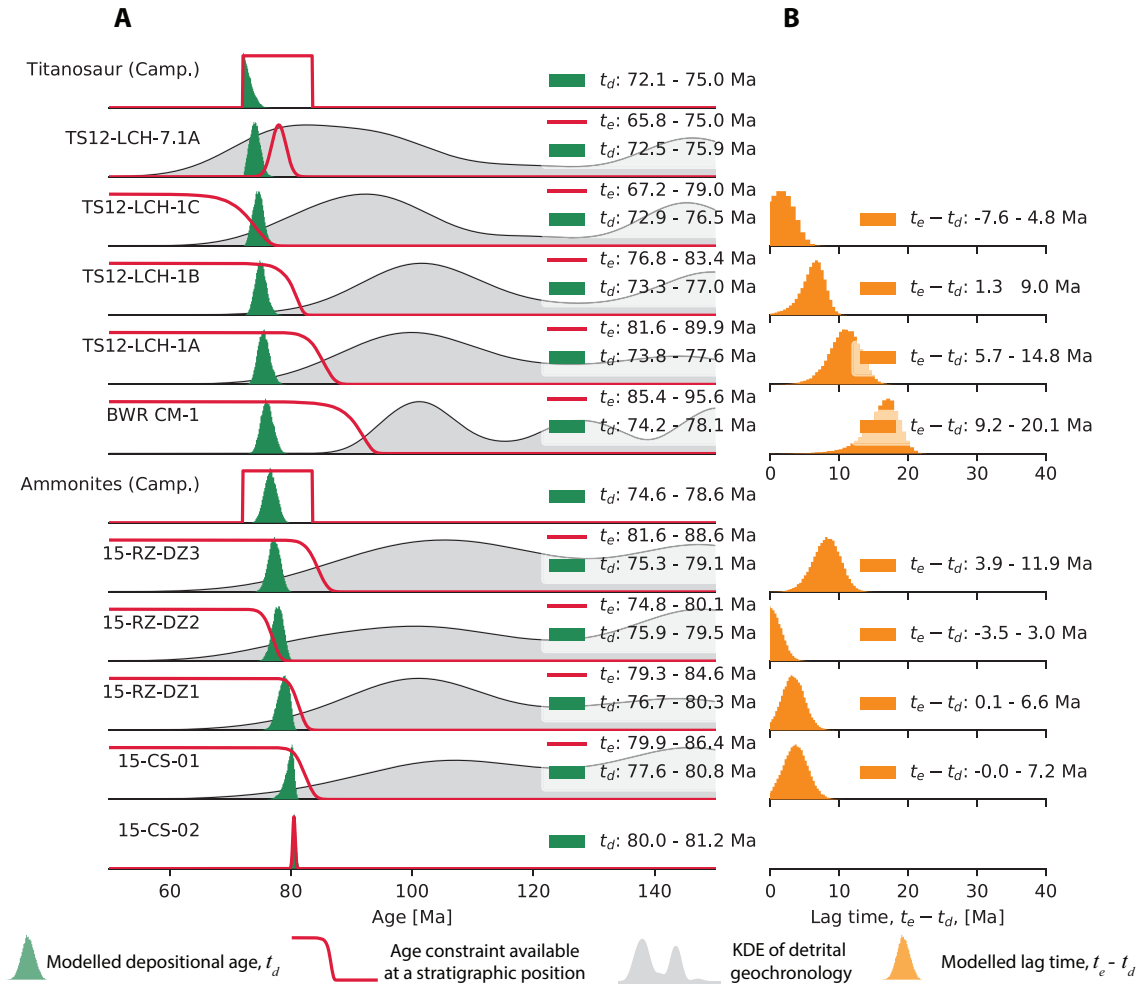


Figure 7: Results of modeling the ages of stratigraphic units from the lower half of the study section (Fig. 6). Each row shows one of the stratigraphic units that contains an age constraint. Age constraints and modelled ages are shown in column **A**. In **A**, each row shows a KDE constructed with a gaussian kernel with a bandwidth equal to the mean 2σ uncertainty of samples if that row corresponds to a detrital geochronology sample, the *likelihood* of a depositional age given the data available for that deposit as a red line, and the *posterior* probability of the depositional age of that unit as a green histogram of MCMC samples with 50 evenly spaced bins. In each plot, the legend indicates the 95% credible interval for the modelled true depositional age t_d and, for detrital geochronology samples, the MDA, t_e , determined with the approach of Keller et al. (2018). For those samples where we compute t_e , column **B** highlights the duration between the modelled timing of last crystallization (t_e) and the modelled timing of deposition (t_d), referred to here as ‘lag time’ (Brandon and Vance, 1992; Romans et al., 2016).

429 We begin by investigating the impacts of enforcing stratigraphic ordering (Eqn. 2) on the
 430 modeled depositional ages of the lower approximately 1,500 m of the Tres Pasos-Dorotea succession
 431 (Tres Pasos slope clinofolds through Dorotea delta-front clinofolds, samples 15-CS-02 through the
 432 Titanosaur observation above TS12-LCH-7.1A; Fig. 6). This lower part of the Tres Pasos-Dorotea
 433 succession is bracketed by absolute age constraints. At the base, sample 15-CS-02 is an ash with
 434 13 zircons dated by isotope dilution-thermal ionization mass spectrometry (ID-TIMS, Daniels
 435 et al., 2018a). At the top, sample TS12-LCH-7.1A is a detrital sample with 99 zircons dated by
 436 LA-ICP-MS (Schwartz et al., 2017). Based on the sedimentological characteristics of the sampled
 437 bed, its modal composition, and the presence of 21 zircon grains defining an indistinguishable,

438 young population, [Schwartz et al. \(2017\)](#) interpreted this unit to be a fluviually reworked ash. We
439 follow the interpretation of [Schwartz et al. \(2017\)](#) and assume that the youngest grain ages in
440 this deposit are syndepositional, such that their age characterizes the true depositional age (i.e.,
441 although it is a detrital sample, it is treated as an ash). In the middle of this sub-section, at
442 the transition from Tres Pasos slope clinofoms to Dorotea delta-front clinofoms, an ammonite
443 fossil assemblage restricts the timing of deposition to Campanian (72.1 - 83.6 Ma; age bounds after
444 [Walker et al., 2018](#)). A Titanosaur fossil at the top of this sub-section further restricts deposition
445 to within the Campanian. Based on these fossil assemblages, we treat the *likelihood* of an age of
446 this unit (Eqn. 1), that is the probability of the observation of this fossil assemblage given an age
447 for the unit, as equally likely within the range 72.1 - 83.6 Ma and impossible outside this range
448 (Fig. 7). As discussed above, this *likelihood* is in no doubt an oversimplification, but nonetheless
449 provides a starting point for incorporating these data. Within this lower interval, eight other
450 detrital zircon samples provide additional age constraints (Fig. 7). We describe the *likelihood* of
451 a true depositional age at the stratigraphic height associated with each of these detrital samples
452 with Equation 9. We refer to the modeled ages of this stratigraphy later in the text as the ‘well
453 constrained’ age only model.

454 We initialize the model with random parameter guesses that obey stratigraphic ordering and
455 are within the intervals allowed by overlying, underlying, and local information (e.g., within the
456 interval bound by the grey regions in Fig. 1). From our initial estimates, we run the MCMC
457 model for 4,000 iterations after an initial burn-in period of 1,000 iterations with 300 walkers.
458 Examination of the results with these parameters shows that this number of iterations allows the
459 model to explore the allowable parameter space during the burn-in phase of the model, so that the
460 post burn-in iterations reflect a stable sampling of the *posterior* distribution.

461 3.2.1 Results and discussion

462 Histograms of the MCMC samples for the depositional ages model after the burn-in period, which
463 approximate the *posterior* probabilities of depositional ages, are shown in Figure 7 A. We summa-
464 rize the MCMC samples for each depositional age (t_d) and MDA (t_e) with the 95% credible interval
465 approximated by the MCMC samples. The modelled ages for all units are limited to fairly precise
466 ranges (95% credible intervals span \sim 3-4 Ma) despite limited absolute age constraints. As was
467 highlighted by Figure 5 C & D, this is a function of the strong age constraints that are available
468 within this section. At the base of the section, the high-precision ID-TIMS date ([Daniels et al.,](#)
469 [2018a](#)) provides a narrow range of allowable ages, and the identified fossil assemblages ([Schwartz](#)
470 [et al., 2017](#)) provide lower limits to depositional ages close to the MDAs.

471 Even though modelled MDAs do not get consistently younger up-section (Fig. 7 A), our
472 stratigraphic constraint (Eqn. 2) enforces this behavior in the modeled true depositional ages. This
473 is highlighted by directly computing a *posterior* probability distribution on the ‘lag-time’ between
474 the time of last zircon crystallization and the timing of deposition in the unit of interest (ignoring
475 that in some instances those youngest zircons could have been recycled from other sedimentary
476 units) ([Brandon and Vance, 1992](#); [Romans et al., 2016](#)). We compute distributions of lag-time by
477 differencing the MCMC sampled distributions of t_e and t_d (an approach similar to [Kruschke, 2013](#)).
478 The lower three detrital zircon samples have lag-times of a few million years or less, but lag-time
479 increases substantially for sample BWR CM-1 (to greater than 10 Ma), and then decreases again
480 towards a few million years or less moving up in the section (Fig. 7 B).

481 The computed 95% credible intervals of lag time include and extend beyond zero in samples
 482 TS12-LCH-1C and 15-RZ-DZ2. Negative lag-times are not possible. The presence of negative
 483 lag-times here reflects that we compute our MDA and t_d independently of one another, and that
 484 the uncertainty in the independently calibrated MDA allows for overlap with the modelled true
 485 depositional age. In other words, these models suggest nearly synchronous crystallization and
 486 deposition of the youngest grains in these samples, but uncertainty in measured ages can result in
 487 some dated grains whose age are less than the depositional age (Coutts et al., 2019).

488 3.3 Modeling the accumulation of sediment as a prograding shelf-slope 489 system

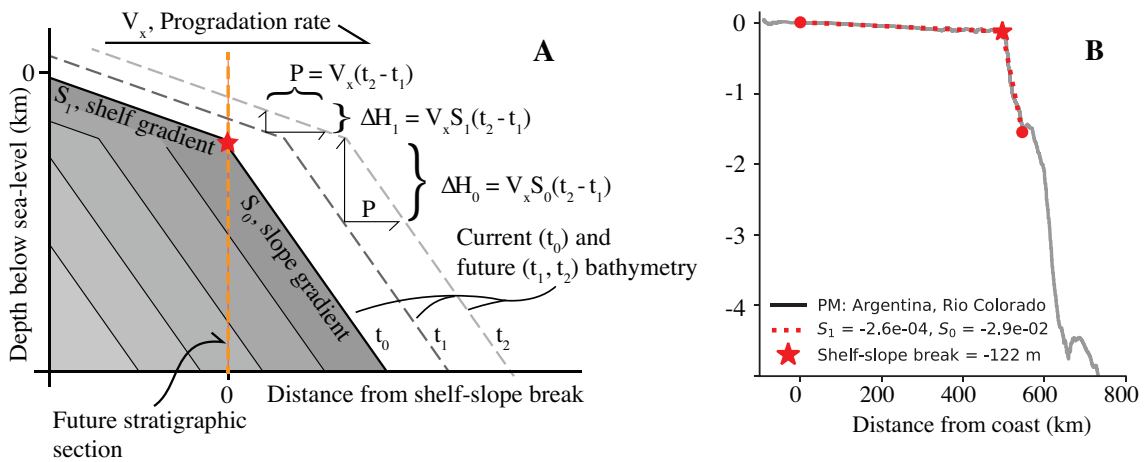


Figure 8: Conceptual model of the accumulation of the Tres Pasos and Dorotea Formations in the Magallanes basin. **A** schematically depicts the accumulation of strata as the result of a prograding shelf-slope system that is advancing self-similarly through time. In this model, the local magnitude of aggradation ΔH is related to the local progradation P by the gradient of the depositional system. As a result, we expect a decrease in vertical sediment accumulation rates (R) when crossing from the higher-gradient shelf to the lower-gradient slope. **B** depicts the bathymetric profile of a modern shelf-slope system (offshore of Rio Colorado, Argentina) measured from ETOPO1 elevations data (Amante and Eakins, 2009) and highlights our method for aggregating topographic data from modern systems. The thin, grey line is the entire profile we collected, from which we only consider those elevations below sea-level and above 1000 m water depth (indicated by the black line). The thin dashed lines depict the fitted topographic profile, from which we calculate S_1 and S_0 , with the shelf-slope break identified by the star.

490 Previous sedimentology-based studies have interpreted the Tres Pasos and Dorotea Formations
 491 to record a transition from marine to terrestrial environments, represented by progressive shoaling
 492 of slope and shelf deposits (Macellari et al., 1989; Covault et al., 2009; Hubbard et al., 2010;
 493 Schwartz and Graham, 2015; Schwartz et al., 2017). Here, we use this field-based interpretation
 494 to establish further constraints on the history of deposition by modelling the depositional ages
 495 of stratigraphy in the context of a stratigraphic accumulation rate (e.g. Fig. 1 D). In light of
 496 these interpretations, we attempt to describe the depositional history with a simple model of the
 497 stratigraphic accumulation rate as expected for a steadily prograding shelf-slope system (Fig. 8
 498 A). Specifically, we model a change in accumulation rate that may be expected to occur with the
 499 transition from deposition on the continental slope recorded by the lower portion of the section, to
 500 deposition on the shelf recorded by the upper portion of the section (e.g., Carvajal and Steel, 2009;
 501 Schwartz et al., 2017). Consider a stratigraphic succession being deposited at the 0 coordinate of

502 the x-axis in Figure 8 A. As the simplified and idealized shelf-slope system progrades self-similarly
 503 out into the basin and over this point, indicated by the star, aggradation will first occur quickly due
 504 to the steep gradient of the slope, and will then slow once that point is overtaken by the prograding
 505 shelf (at which point we would also expect a change in depositional environment). We simplify this
 506 depositional history by expressing this progradation with two stratigraphic accumulation rates, R_0
 507 and R_1 , which respectively represent deposition on the slope and shelf,

$$H(t) = \begin{cases} H = R_0(t - t_0), & \text{if } H < H_c \\ H = H_c + R_1(t - t_c), & \text{otherwise.} \end{cases} \quad (10)$$

508 Here, H_c is the height in the stratigraphic section where deposition rates slow from R_0 to R_1 ,
 509 which is derived based on the time that deposition on the continental shelf begins, t_c ,

$$H_c = R_0(t_c - t_0). \quad (11)$$

510 Given steady, self-similar progradation of a shelf-slope system (Fig. 8), the rates R_0 and R_1
 511 can be considered to be the product of the local depositional gradients, S , and the progradation
 512 rate, V_x ,

$$R_0 = V_x S_0, R_1 = V_x S_1. \quad (12)$$

513 From this, we see that we would expect the ratio of accumulation rates to be equivalent to the
 514 ratio of depositional gradients on the shelf, S_1 , and slope, S_0 :

$$\frac{R_0}{R_1} = \frac{V_x S_0}{V_x S_1} = \frac{S_0}{S_1} \quad (13)$$

515 While we may have little prior knowledge regarding the deposition rates in the Magallanes basin,
 516 if that depositional system was similar to those on earth today, we can make a good prediction
 517 of $\frac{S_0}{S_1}$ based on the ratio of depositional gradients observed in modern shelf-slope systems. If the
 518 assumptions made in deriving Eqn. 13 are valid, then the ratio of modern shelf-slope gradients (Fig.
 519 8 B) can provide insight into how much accumulation rates may have changed when transitioning
 520 from deposition on the slope to deposition on the shelf. We can insert this expectation into our
 521 model of stratigraphic accumulation rates in the form of a statement about *prior* probability in
 522 Bayes' rule (Eqn. 1).

523 To develop our expectation of $\frac{S_0}{S_1}$, we compiled 45 bathymetric profiles across modern shelf-
 524 slope breaks from ETOPO1 elevation data (Amante and Eakins, 2009) using Google Earth Engine
 525 (Gorelick et al., 2016). Profiles were selected in order to provide an adequate representation of
 526 the variation in shelf-slope morphologies using the following criteria: 1) all profiles were collected
 527 from siliciclastic-dominated systems (i.e., excluding high-relief carbonate banks, etc.); 2) the set
 528 of profiles is affected by a spectrum of wave-, tide-, and river-associated processes, but with a
 529 preference for fluvial input at the shoreline to mimic the Magallanes basin example; 3) all profiles
 530 extend across the entire shelf, include the shelf-slope break, and end at the approximate base-of-
 531 slope; and 4) no profiles cross plate boundaries, but may be closely associated with one. Between
 532 sea-level and depths of 1,500 m, we fit a piece-wise linear-regression by minimizing the sum of the

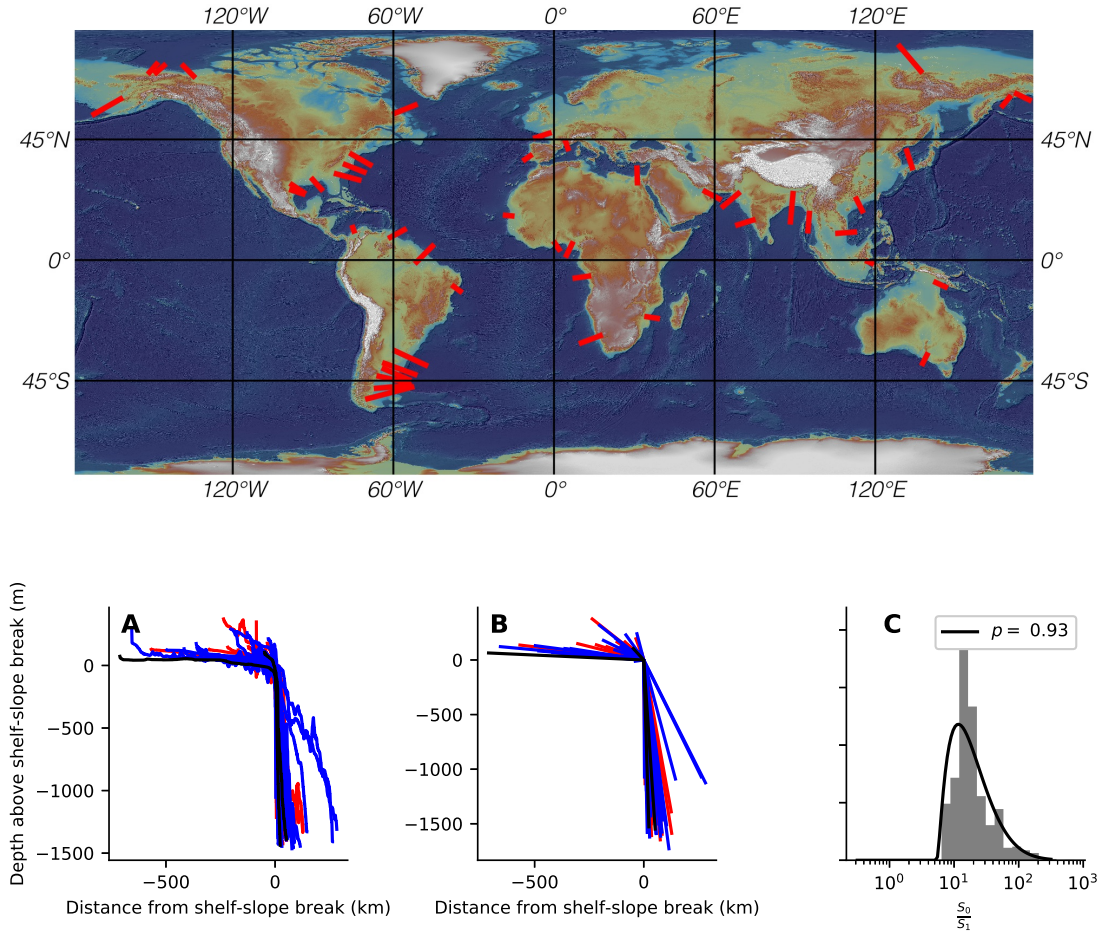


Figure 9: . Compilation of observations from 45 modern shelf-slope systems. Map of shaded relief topography from ETOPO1 elevation data (Amante and Eakins, 2009) shows the locations of extracted bathymetric profiles in red. The bottom row **A-C** shows the data extracted from the profiles. **A** is a composite of all profiles of bathymetry collected from ETOPO1 elevation data (Amante and Eakins, 2009), hung so that 0,0 is at the best fit shelf-slope break. **B** depicts all of the simplified topographic fits for the profiles. In **A** and **B**, red, blue, and black lines indicate profiles from convergent, passive, and rifted margins, respectively. **C** depicts the ratio of slope to shelf gradients (e.g. Eqn. 13), with the thin black line indicating the best fitting distribution of relative gradients of the slope and shelf. Under the assumption that progradation of a similar system was steady, and occurred self-similarly, we use this distribution to characterize the *prior* probability on the ratio of accumulation rates on the slope and shelf, $\frac{R_0}{R_1}$. The K-S test does not reject the null hypothesis that the observations of shelf-slope data were drawn from this distribution ($p = 0.93$).

533 squared errors between that fitted surface and the topography (Fig. 8 B). This regression intends
 534 to mimic a simple slope break where the average bathymetric gradient transitions from shallow
 535 to steep, a kinked topographic surface representing a simplified shelf-slope geometry (Fig. 8). All
 536 extracted topographic profiles are shown in Figure 9 A, with their best-fitting counterparts shown
 537 in Figure 9 B. In these plots we stack all the data so that 0 on the x- and y-axes is at the shelf-slope
 538 break.

539 The ratio of shelf to slope gradients, $\frac{S_0}{S_1}$ (Figs. 8 & 9 C), is well described by a log-normal
 540 distribution with a shape $\sigma_R = 1.2$, location, $\theta_R = 5.3$, and scale, $m_R = 29.4$, so we take this as

541 the *prior* probability of the ratio of accumulation rates ($\frac{R_0}{R_1}$),

$$P(R_0, R_1) = \frac{1}{\left(\frac{R_0}{R_1} - \theta_R\right)\sigma_r\sqrt{2\pi}} e^{-\frac{\ln\left(\frac{R_0}{R_1} - \theta_R\right)/m_r}{2\sigma_R^2}}. \quad (14)$$

542 From stratigraphic observations we also have expectations of where in the section we expect strati-
543 graphic accumulation rates to transition from R_0 to R_1 (that is, the stratigraphic height, H_c in
544 Eqn. 10). There is a lithofacies transition between Dorotea delta-front clinofolds and Dorotea
545 delta plain deposits at approximately 1450 m in the examined section (after Schwartz et al., 2017).
546 Since the Dorotea delta-front was attached to the shelf-edge (i.e., a shelf-edge delta) (Schwartz and
547 Graham, 2015; Schwartz et al., 2017), the lithofacies transition from delta-front to delta-plain can
548 effectively be considered to represent a change from slope-dominant deposition to shelf-dominant
549 deposition. Defining a continuous *prior* probability on H_c is more challenging than it was for $\frac{R_0}{R_1}$,
550 where that probability function was dictated by a large number of observations.

551 The transition in lithofacies used to define H_c at 1450 m occurs within an approximately 150
552 m-thick succession of sandstone and conglomerate that represents tidally influenced mouth bars
553 and distributary channels (e.g., facies assemblage 3 after Schwartz et al., 2017). We select the
554 parameters of a t distribution describing H_c to conservatively match the scale of this lithofacies
555 unit (Schwartz et al., 2017). Specifically, this is done so that the 95% confidence interval ranges 100
556 m on either side of 1450 m transition (encompassing the majority of the delta-front interval) and
557 that the 99% confidence bounds extend an additional 150 m beyond this (extending an additional
558 thickness of this lithofacies beyond the 95% interval). This is accomplished with a t distribution
559 with a location, μ of 1450, a scale, σ of 25, and a value of v of 2. We utilize a t distribution to
560 describe our *prior* probability on H_c because the broad tails allow us to acknowledge that this
561 identification was subjective and that the model should be able to explore values well outside of
562 our assigned central value. Although v typically denotes the degrees of freedom, we instead use
563 it here as a ‘normality’ parameter (Kruschke, 2013); smaller values of v expand the tails of this
564 distribution and cause it to deviate from a normal distribution.

565 From our initial estimates, we run the MCMC model for 5,000 iterations after an initial burn-
566 in period of 500 iterations with 400 walkers. We use a starting guess of $t_0 = 79.5$, of R_0 & $R_1 =$
567 $-1,000$ & -95 and $t_1 = 78.0$, as these are consistent with our priors and able to predict ages for all
568 deposits with temporal constraints. The negative values of R indicate that strata accumulate as
569 ages decrease. We start each walker with initial guesses drawn from a normal distribution with
570 the previously mentioned means and a 0.1% relative error. From these initial guesses the MCMC
571 model is able to expand to a stable sampling space over the burn-in period.

572 3.3.1 Results and discussion

573 Results for the model of stratigraphic accumulation rates are shown in Fig. 10, which highlights
574 both the modeled depositional ages and the modeled stratigraphic accumulation rate curve from
575 which these ages are derived. For each age, we report the 95% credible interval derived from the
576 MCMC samples. All of the geochronologic constraints can be appropriately described by a ‘kinked’
577 stratigraphic accumulation rate that transitions from a relatively rapid accumulation rate to a
578 slower one at $H_c = 1456$ (+100, -104) m (reported as the median and the range between the 5th and
579 95th percentiles of the MCMC samples characterizing the posterior), approximately the position

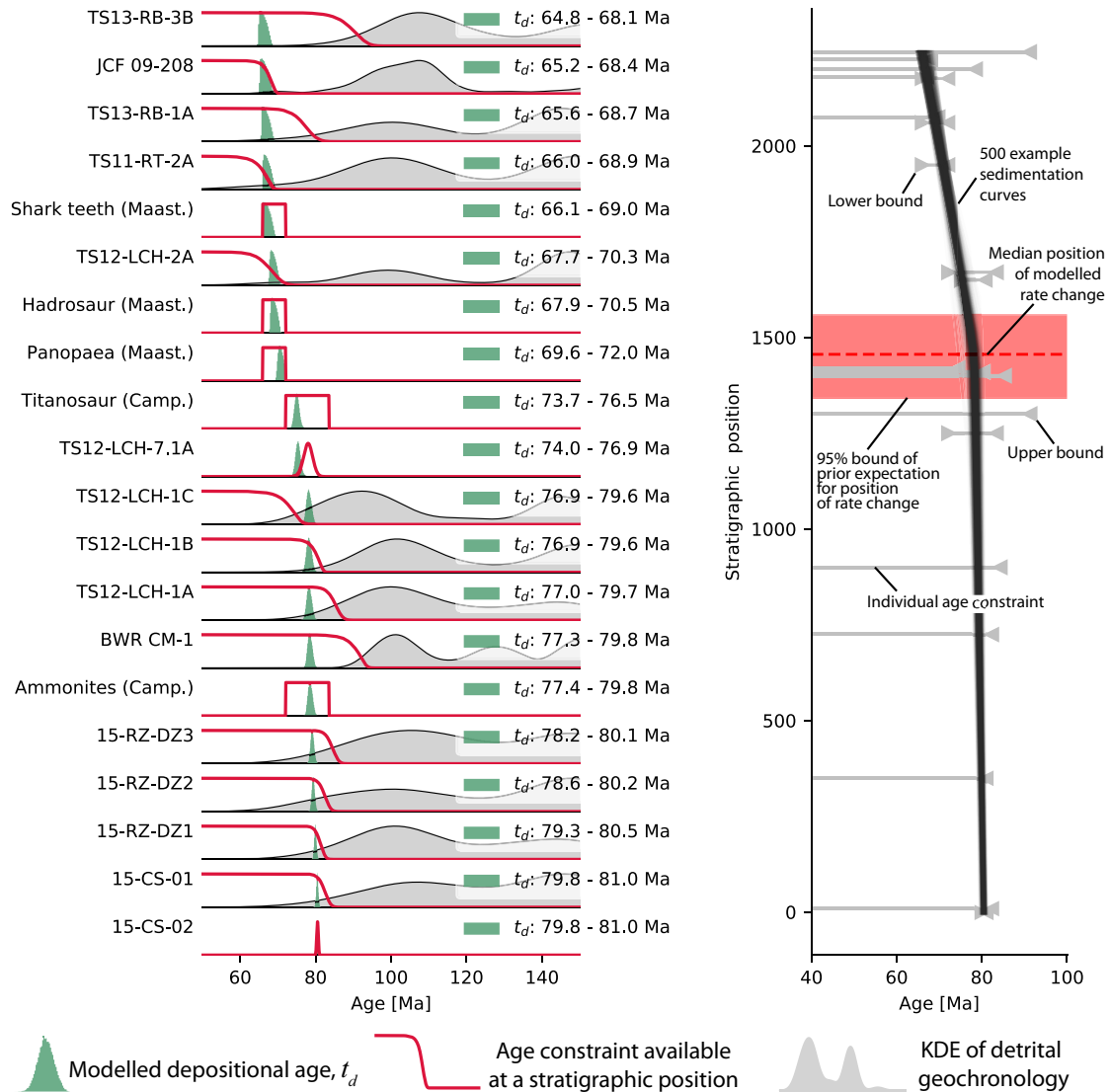


Figure 10: Results of modeling the stratigraphic accumulation rate of the Magallanes basin based on geochronologic constraints. Each row shows a KDE constructed with a gaussian kernel with a bandwidth equal to the mean 2σ uncertainty of samples if that row corresponds to a detrital geochronology sample, the *likelihood* of a depositional age given the data available for that deposit as a red line, and the *posterior* probability of the depositional age of that unit as a green histogram of MCMC samples with 50 evenly spaced bins. In each of these plots the legend indicates the 95% credible interval for the modelled true depositional age, t_d and, for detrital geochronology samples, the MDA, t_e , determined with the approach of Keller et al. (2018). Right panel depicts the allowable ranges of ages for each sample, shown by grey horizontal lines, positioned vertically at their respective stratigraphic positions and extending horizontally from the point at which the *likelihood* function exceeds 1% of its mass to the point where it decreases below 1% of its mass; note that the age constraints are not distributed equally throughout the section. The grey horizontal age constraints do not factor in the geologic constraint imposed by superposition. Stacked, semi-transparent black lines are a subset of the probable stratigraphic accumulation rate solutions drawn from the MCMC samples. Red dashed line and box indicate the median modelled position of a change in sediment accumulation rate and the 95% bound of our prior expectation based on facies transitions (Schwartz and Graham, 2015).

580 of a change in depositional facies (Fig. 6 & 10). The lower, more rapid sediment accumulation
 581 rate $R_0 = -675$ (-1031, +227) m/Ma, we associate with progradation of the Tres Pasos slope. The
 582 slower accumulation rate in the upper part of the section, $R_1 = -65$ (-14, +11) m/Ma, we associate

583 with the Dorotea delta-plain (Fig. 6). Based on the relative gradients in modern systems $\frac{S_0}{S_1}$ (Fig.
584 9), we expect the ratio of accumulation rates in self-similarly propagating shelf-slope systems, $\frac{R_0}{R_1}$,
585 to be 11.7. This is similar to the median *posterior* value of 10.3 observed from our model of the
586 Magallanes basin. In summary, the available geochronologic data are not sufficient to provide a
587 substantive update of our *prior* knowledge of H_c , resulting in a nearly identical *posterior*. Similarly,
588 there is much overlap between the *prior* and *posterior* distributions on relative rates $\frac{R_0}{R_1}$, but the
589 *posterior* distribution indicates a much lower probability of relative rates greater than 30 than was
590 suggested by our *prior* expectations that were derived from measurements of modern bathymetry
591 (Fig. 9 & 11). In other words, given our model of stratigraphic accumulation rates (e.g. Fig. 8
592 A), the ratio of stratigraphic accumulation rates for the Magallanes basin is not expected to be as
593 high as the ratio of shelf to slope gradients observed in many modern systems. However, the most
594 likely value of $\frac{R_0}{R_1}$ (Fig. 11) is very similar to the most common observation of $\frac{S_0}{S_1}$ from modern
595 systems (Fig. 9)

596 Alternative depositional histories could also explain the observed geochronology. One such
597 explanation would be the presence of an unconformity at approximately 1670 m (the location of
598 the observed Titanosaur), above and below which point all geochronologic constraints could be
599 described by a near-instantaneous rate of deposition (Fig. 10). In this model, one could effectively
600 describe the observed geochronology with three variables; an age of material below an unconfor-
601 mity, above the unconformity, and the duration of the unconformity. Although an unconformity
602 separating two rapidly deposited accumulations of sediment could explain the geochronologic data
603 from the Magallanes basin (Fig. 10), the detailed observational record does not currently support
604 this. No major erosion surfaces, well developed soils, or dramatic changes in lithofacies have been
605 observed in this interval (Schwartz and Graham, 2015). While the models introduced here pro-
606 duce predictions of deposit ages that are subject to our interpretations of the geologic record, it is
607 for that same reason that we argue they are constructive, as they provide testable prediction for
608 our hypotheses of geologic histories. In the case presented here, the available geochronology can
609 not refute those predictions.

610 Our model of stratigraphic accumulation rate is derived from the expectation that the stratigra-
611 phy represents steady, uninterrupted progradation of a shelf-slope system through the Magallanes
612 foredeep on a multi-Myr scale. This assumption for the model is consistent with observed strati-
613 graphic patterns that suggest 1) progressive southward progradation of the shelf and slope in Late
614 Cretaceous time; 2) maintained genetic linkage between the Dorotea shelf and Tres Pasos slope (at
615 least at the scale of outcrop exposure); and 3) a lack of significant unconformities within the Tres
616 Pasos-Dorotea succession (Romans et al., 2010; Hubbard et al., 2010; Schwartz and Graham, 2015;
617 Schwartz et al., 2017; Daniels et al., 2018a). We note that this is a highly simplified model that
618 does not account for sub-Myr sedimentary processes (e.g., deltaic lobe-switching), variable sub-
619 sidence patterns, or compaction (which could preferentially impact the finer grain sizes observed
620 on the slope, and thus produce values of $\frac{S_0}{S_1}$ larger than $\frac{R_0}{R_1}$, similar to what we observe here).
621 Rather, this model is an assumption of long-term (multi-Myr), "average" sedimentation patterns
622 consistent with a highly generalized interpretation of the stratigraphy (e.g., Fig. 6 B & 8, after
623 Schwartz et al., 2017).

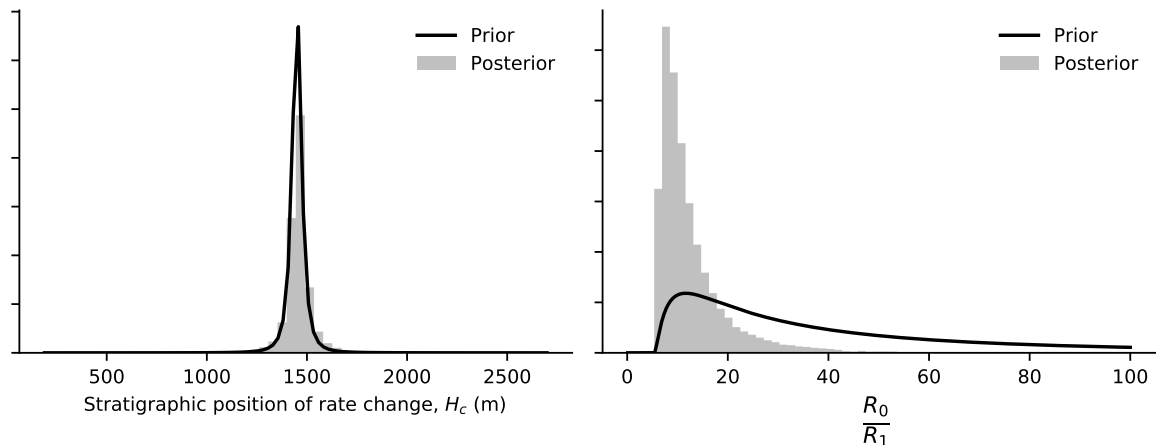


Figure 11: *Prior* and *posterior* probabilities (e.g. our initial knowledge and modeled inference) on the stratigraphic position of a change in rate (H_c) and the relative stratigraphic accumulation rates above and below that transition. *Prior* distributions are shown as solid black lines, *posterior* distributions are shown as normalized histograms of MCMC samples after the burn-in period.

624 4 Discussion and Conclusion

625 Sedimentary deposits are no older than their youngest mineral constituent, and efforts to calculate
626 maximum depositional ages from detrital geochronology often rely on weighted means that are
627 calculated based on defined groups of young grains (see [Coutts et al., 2019](#), and references therein).
628 Given the typical numbers of grains analyzed in detrital zircon geochronology studies ($n \sim 100$,
629 [Coutts et al., 2019](#); [Sharman et al., 2018](#)), we can be fairly certain that we will capture at least
630 three grains from the youngest population if that population comprises $\sim 10\%$ of all zircons (Fig.
631 2, see [Andersen, 2005](#), for a more complete discussion). However, caution should be taken as this
632 limits how often we should expect to see certain rare, young populations. Only in $\sim 10\%$ of studies
633 of 100 grains would we expect to date three of the youngest grains if grains of that age only made
634 up $\sim 1\%$ of dateable zircons.

635 Superposition (or any cross cutting relationship) provides an additional constraint on the ages
636 of deposits. Utilizing Bayesian statistics to enforce this principle has long been a tactic of ar-
637 chaeological and paleoenvironmental studies that infer depositional ages from geochronologic data
638 (e.g., [Naylor and Smith, 1988](#); [Buck et al., 1992](#); [Christen et al., 1995](#); [Blaauw and Christen,](#)
639 [2005](#); [Parnell et al., 2008](#); [Haslett and Parnell, 2008](#); [Bronk Ramsey, 2009](#); [Blaauw, 2010](#); [Blaauw](#)
640 [and Christeny, 2011](#)). Given some additional constraints that provide minimum limiting ages for
641 deposits, these Bayesian approaches can be used to determine true depositional ages for deposits
642 where only maximum depositional age constraints are present. While it is straightforward enough
643 to qualitatively interpret ages with stratigraphic relationships in mind, placing these in a Bayesian
644 framework enables inference of true depositional ages and their uncertainties (e.g., Fig. 5). In spite
645 of variations in the lag time between crystal formation and deposition, this approach makes pre-
646 dictions for the depositional ages of samples from the Magallanes basin with credible age intervals
647 that span ~ 4 Ma (Fig. 7). While we achieve this degree of precision with limited direct constraints
648 on depositional ages, this is also a favorable example. Situations with greater uncertainties on the
649 samples that are directly dated or larger gaps between the youngest ages of zircons low in the
650 section and constraints that provide lower limits on ages high in the sections will be met with

651 greater uncertainty (Fig. 1).

652 Here we determine age constraints, and assign the *likelihood* of depositional ages for each de-
653 posit, independently of modelling true depositional ages. The independence of these two steps
654 results in some distributions of lag time that unrealistically span 0 Ma (Fig. 7 B). Future efforts
655 can improve upon this by simultaneously solving for MDAs and t_d and, for example, enforcing the
656 *prior* expectation that $t_e > t_d$. Such an approach might enable greater confidence in MDAs that
657 depended on a small number of grains, as it would require these MDAs be consistent with other
658 information in the stratigraphic section and therefore could help to reject observations from incon-
659 sistent grains that might be the product of contamination or Pb loss. The *posterior* probabilities
660 of depositional ages inferred here are dependent on our characterization of the *likelihood* of a true
661 depositional age given a suite of detrital geochronology ages (Eqn. 7 & Fig. 4). Rather than
662 the method of estimating t_e that we apply here (Keller et al., 2018), another alternative would
663 be to determine the most likely true ages contained within a detrital geochronology sample using
664 a mixture modelling approach that placed emphasis on identification of the youngest component
665 (Vermeesch, 2018). The youngest true component age determined by the mixture model, and its
666 uncertainty, could then be used to define the *likelihood* of a true depositional age (Eqn. 9).

667 Describing the entire stratigraphic section with a sedimentation rate curve provides a way to
668 propagate age constraints to samples at the top of a stratigraphic section that are only charac-
669 terized by MDAs (Fig. 10). In our example from the Magallanes basin, the uppermost four age
670 constraints are all obtained from detrital zircon analyses. Had we viewed these samples individu-
671 ally, each of them could be well described by any age < 92 Ma, but given our model of stratigraphic
672 accumulation rate, the uppermost unit (TS13-RB-3B) has a predicted age of 64.8-68.1 Ma. Here
673 we prescribe the form of this sedimentation rate curve in order to replicate expectations from a
674 simple conceptual model of a prograding shelf-slope break (Fig. 8). This in turn allows us to
675 inform our inference of ancient deposition rates with expectations derived from measurements of
676 modern depositional systems (Fig. 9). Rather than specifying a form to the deposition rate curve,
677 there are many existing tools for more flexibly determining how sedimentation rates might vary
678 through time, some of which can also enable introduction of expectations of hiatuses or inflections
679 in deposition rates derived from sedimentologic observations (e.g., Blaauw and Christen, 2005;
680 Parnell et al., 2008; Haslett and Parnell, 2008; Bronk Ramsey, 2009; Blaauw, 2010; Blaauw and
681 Christeny, 2011).

682 Our model of sedimentation rates (Fig. 10) produces parameter estimates that overlap signifi-
683 cantly with the *prior* expectations we derive based on sedimentology (Schwartz et al., 2017) and
684 measurements of modern depositional systems (Fig. 9 & 11). It is easy to imagine two seemingly
685 conflicting interpretations of the observation that the *posterior* probabilities significantly overlap
686 the *prior* probabilities: (1) that through asserting these *prior* probabilities we have forced a partic-
687 ular outcome, or (2) that the data we do have is consistent with our expectations for this system.
688 A more conservative statement would be to acknowledge both points: the available geochronologic
689 constraints do not provide information that is either contrary to our expectation or in support
690 of a more precise quantification of the rates of stratigraphic accumulation or the point in the
691 stratigraphic section at which they change.

692 The probabilities of ages we report here (Fig. 7 & 10) are explicitly linked to the model
693 that generated them. As a result, model ages covary with one another. In the stratigraphic
694 accumulation model (Fig. 10), the detrital zircon sample from sedimentary unit 15-CS-01 that

695 immediately overlies the ID-TIMS dated ash sample 15-CS-02 has a similarly precise *posterior*. We
696 do not take that to mean that the timing of deposition is equally well-known for both samples;
697 rather, this implies that both samples are similarly constrained given our model of the deposition
698 history. In general, we have attempted to show how coupling geologic insights with geochronology
699 can improve our understanding of sedimentary sections and can expand the inferences we can make
700 from sections with detrital records of maximum depositional ages. The routine practice in geology
701 of enforcing stratigraphic order in interpretation of the ages of deposits from MDAs is inherently
702 Bayesian. Building this knowledge into a statistical model can provide a cascade of information
703 through series of samples that can improve our characterization of geologic histories.

704 5 Acknowledgements

705 We thank L.E. Morgan for introduction to the concept of enforcing stratigraphic ordering into
706 geochronology data. Early conversations with G. Sharman and M. Malkowski inspired this manuscript
707 and discussion with S. Hubbard and D. Coutts provided further insights into maximum depositional
708 ages. Editorial comments from B. Romans and two anonymous reviews substantively improved the
709 clarity and direction of this manuscript. Support for this work came from the FEDMAP compo-
710 nent of the US Geological Survey National Cooperative Geologic Mapping Program and from the
711 Mineral Resources Program. Any use of trade, firm, or product names is for descriptive purposes
712 only and does not imply endorsement by the U.S. Government.

713 References

- 714 Amante, C. and Eakins, B. (2009). ETOPO1 1 Arc-Minute Global Relief Model: Procedures, Data
715 Sources and Analysis.
- 716 Amidon, W. H., Burbank, D., and Gehrels, G. (2005). U–Pb zircon ages as a sediment mixing
717 tracer in the Nepal Himalaya. *Earth and Planetary Science Letters*, 235(1-2):244–260.
- 718 Andersen, T. (2005). Detrital zircons as tracers of sedimentary provenance: Limiting conditions
719 from statistics and numerical simulation. *Chemical Geology*, 216(3-4):249–270.
- 720 Bernhardt, A., Jobe, Z. R., and Lowe, D. R. (2011). Stratigraphic evolution of a submarine
721 channel-lobe complex system in a narrow fairway within the Magallanes foreland basin, Cerro
722 Toro Formation, southern Chile. *Marine and Petroleum Geology*, 28(3):785–806.
- 723 Biddle, K. T., Uliana, M. A., Mitchum, R. M., Fitzgerald, M. G., and Wright, R. C. (1986).
724 The stratigraphic and structural evolution of the central eastern Magallanes Basin, southern
725 South America. 41–61. *Foreland basins. International Association of Sedimentologists, Special
726 Publication*, 8:453.
- 727 Blaauw, M. (2010). Methods and code for ‘classical’ age-modelling of radiocarbon sequences.
728 *Quaternary Geochronology*, 5(5):512–518.
- 729 Blaauw, M. and Christen, J. A. (2005). Radiocarbon peat chronologies and environmental change.
730 *Journal of the Royal Statistical Society: Series C (Applied Statistics)*, 54(4):805–816.

- 731 Blaauw, M. and Christeny, J. A. (2011). Flexible paleoclimate age-depth models using an autore-
732 gressive gamma process. *Bayesian Analysis*, 6(3):457–474.
- 733 Brandon, M. T. and Vance, J. A. (1992). Tectonic evolution of the Cenozoic Olympic subduction
734 complex, Washington State, as deduced from fission track ages for detrital zircons. *American*
735 *Journal of Science*, 292(8):565–636.
- 736 Bronk Ramsey, C. (2009). Bayesian Analysis of Radiocarbon Dates. *Radiocarbon*, 51(01):337–360.
- 737 Buck, C. E., Litton, C. D., and Smith, A. F. (1992). Calibration of radiocarbon results pertaining
738 to related archaeological events. *Journal of Archaeological Science*, 19(5):497–512.
- 739 Carvajal, C. and Steel, R. (2009). Shelf-Edge Architecture and Bypass of Sand to Deep Water:
740 Influence of Shelf-Edge Processes, Sea Level, and Sediment Supply. *Journal of Sedimentary*
741 *Research*, 79(9):652–672.
- 742 Christen, J. A., Clymo, R. S., and Litton, C. D. (1995). A Bayesian Approach to the Use of ^{14}C
743 Dates in the Estimation of the Age of Peat. *Radiocarbon*, 37(02):431–441.
- 744 Coutts, D. S., Matthews, W. A., and Hubbard, S. M. (2019). Assessment of widely used methods
745 to derive depositional ages from detrital zircon populations. *Geoscience Frontiers*, in press.
- 746 Covault, J. A., Romans, B. W., and Graham, S. A. (2009). Outcrop Expression of a Continental-
747 Margin-Scale Shelf-Edge Delta from the Cretaceous Magallanes Basin, Chile. *Journal of Sedi-*
748 *mentary Research*.
- 749 Dalziel, I. W., De Wit, M. J., and Palmer, K. F. (1974). Fossil marginal basin in the southern
750 Andes. *Nature*.
- 751 Dalziel, I. W. D. (1981). Back-Arc Extension in the Southern Andes: A Review and Critical
752 Reappraisal. *Philosophical Transactions of the Royal Society A: Mathematical, Physical and*
753 *Engineering Sciences*.
- 754 Daniels, B. G., Auchter, N. C., Hubbard, S. M., Romans, B. W., Matthews, W. A., and Stright, L.
755 (2018a). Timing of deep-water slope evolution constrained by large-n detrital and volcanic ash
756 zircon geochronology, Cretaceous Magallanes Basin, Chile. *Bulletin of the Geological Society of*
757 *America*, 130(3-4):438–454.
- 758 Daniels, B. G., Kaempfe, S., Hubbard, S. M., Romans, B. W., and Matthews, W. A. (2018b). The
759 influence of Andean orogenic uplift and deformation style on the evolution of stratigraphic archi-
760 tecture, Cretaceous Magallanes foreland basin, Chilean Patagonia. In *XV Congreso Geológico*
761 *Chileno Actas*, page 1156.
- 762 Dickinson, W. R. and Gehrels, G. E. (2009). Use of U-Pb ages of detrital zircons to infer maximum
763 depositional ages of strata: A test against a Colorado Plateau Mesozoic database. *Earth and*
764 *Planetary Science Letters*, 288(1-2):115–125.
- 765 Fildani, A. and Hessler, A. M. (2005). Stratigraphic record across a retroarc basin inversion:
766 Rocas Verdes-Magallanes Basin, Patagonian Andes, Chile. *Bulletin of the Geological Society of*
767 *America*.
- 768 Foreman-Mackey, D., Hogg, D. W., Lang, D., and Goodman, J. (2013). emcee : The MCMC
769 Hammer. *Publications of the Astronomical Society of the Pacific*, 125(925):306–312.

- 770 Fosdick, J. C., Graham, S. A., and Hilley, G. E. (2014). Influence of attenuated lithosphere and
771 sediment loading on flexure of the deep-water Magallanes retroarc foreland basin, Southern
772 Andes. *Tectonics*, 33(12):2505–2525.
- 773 Fosdick, J. C., Romans, B. W., Fildani, A., Bernhardt, A., Calderón, M., and Graham, S. A.
774 (2011). Kinematic evolution of the Patagonian retroarc fold-and-thrust belt and Magallanes
775 foreland basin, Chile and Argentina, 51°30's. *Bulletin of the Geological Society of America*.
- 776 Gorelick, N., Hancher, M., Dixon, M., Ilyushchenko, S., Thau, D., and Moore, R. (2016). Google
777 Earth Engine: Planetary-scale geospatial analysis for everyone. *Remote Sensing of Environment*.
- 778 Haslett, J. and Parnell, A. (2008). A simple monotone process with application to radiocarbon-
779 dated depth chronologies. *Journal of the Royal Statistical Society: Series C (Applied Statistics)*,
780 57(4):399–418.
- 781 Hubbard, S. M., Fildani, A., Romans, B. W., Covault, J. A., and McHargue, T. R. (2010). High-
782 Relief Slope Clinoform Development: Insights from Outcrop, Magallanes Basin, Chile. *Journal*
783 *of Sedimentary Research*.
- 784 Keller, C., Schoene, B., and Samperton, K. (2018). A stochastic sampling approach to zircon
785 eruption age interpretation. *Geochemical Perspectives Letters*, pages 31–35.
- 786 Kruschke, J. K. (2013). Bayesian estimation supersedes the t test. *Journal of Experimental*
787 *Psychology: General*, 142(2):573–603.
- 788 Macellari, C. E., Barrio, C. A., and Manassero, M. J. (1989). Upper cretaceous to paleocene
789 depositional sequences and sandstone petrography of southwestern Patagonia (Argentina and
790 Chile). *Journal of South American Earth Sciences*.
- 791 Malkowski, M. A., Sharman, G. R., Graham, S. A., and Fildani, A. (2017). Characterisation
792 and diachronous initiation of coarse clastic deposition in the Magallanes-Austral foreland basin,
793 Patagonian Andes. *Basin Research*, 29(April 2016):298–326.
- 794 Natland, M. L. (1974). *A system of stages for correlation of Magallanes Basin sediments*, volume
795 139. Geological Society of America.
- 796 Naylor, J. C. and Smith, A. F. M. (1988). An Archaeological Inference Problem. *Journal of the*
797 *American Statistical Association*, 83(403):588–595.
- 798 Parnell, A. C., Buck, C. E., and Doan, T. K. (2011). A review of statistical chronology models for
799 high-resolution, proxy-based Holocene palaeoenvironmental reconstruction. *Quaternary Science*
800 *Reviews*, 30(21-22):2948–2960.
- 801 Parnell, A. C., Haslett, J., Allen, J. R., Buck, C. E., and Huntley, B. (2008). A flexible approach
802 to assessing synchronicity of past events using Bayesian reconstructions of sedimentation history.
803 *Quaternary Science Reviews*, 27(19-20):1872–1885.
- 804 Romans, B. W., Castelltort, S., Covault, J. A., Fildani, A., and Walsh, J. P. (2016). Environmental
805 signal propagation in sedimentary systems across timescales. *Earth-Science Reviews*, 153:7–29.
- 806 Romans, B. W., Fildani, A., Graham, S. A., Hubbard, S. M., and Covault, J. A. (2010). Importance
807 of predecessor basin history on sedimentary fill of a retroarc foreland basin: provenance analysis
808 of the Cretaceous Magallanes basin, Chile (50-52°S). *Basin Research*, 22(5):640–658.

- 809 Schwartz, T. M., Fosdick, J. C., and Graham, S. A. (2017). Using detrital zircon U-Pb ages to
810 calculate Late Cretaceous sedimentation rates in the Magallanes-Austral basin, Patagonia. *Basin*
811 *Research*, 29(6):725–746.
- 812 Schwartz, T. M. and Graham, S. A. (2015). Stratigraphic architecture of a tide-influenced shelf-edge
813 delta, Upper Cretaceous Dorotea Formation, Magallanes-Austral Basin, Patagonia. *Sedimentol-*
814 *ogy*, 62(4):1039–1077.
- 815 Sharman, G. R., Sharman, J. P., and Sylvester, Z. (2018). detritalPy: A Python-based toolset
816 for visualizing and analysing detrital geo-thermochronologic data. *The Depositional Record*,
817 X(June).
- 818 VanderPlas, J. (2014). Frequentism and Bayesianism: A Python-driven Primer. *arXiv*, astro-
819 ph.I(Scipy):1–9.
- 820 Vermeesch, P. (2012). On the visualisation of detrital age distributions. *Chemical Geology*, 312-
821 313:190–194.
- 822 Vermeesch, P. (2018). IsoplotR: A free and open toolbox for geochronology. *Geoscience Frontiers*,
823 9(5):1479–1493.
- 824 Walker, D., Geissman, J., Bowring, S., and Babcock, L. (2018). GSA Geologic time scale v. 5.0.
825 *Geological Society of America*.
- 826 Wilson, T. J. (1991). Transition from back-arc to foreland basin development in the southernmost
827 Andes: Stratigraphic record from the Ultima Esperanza District, Chile. *Geological Society of*
828 *America Bulletin*, 103(1):98–111.